

Handling Missing Modalities in Multimodal Survival Prediction for Non-Small Cell Lung Cancer

Filippo Ruffini^{1,2†}, Camillo Maria Caruso^{1†}, Claudia Tacconi⁴,
Lorenzo Nibid^{5, 6}, Francesca Miccolis¹⁰, Marta Lovino¹⁰,
Carlo Greco^{3, 4}, Edy Ippolito^{3, 4}, Michele Fiore^{3, 4},
Alessio Cortellini^{7,8}, Bruno Beomonte Zobel⁹,
Giuseppe Perrone^{5, 6}, Bruno Vincenzi^{7, 8}, Claudio Marrocco¹¹,
Alessandro Bria¹¹, Elisa Ficarra¹⁰, Sara Ramella^{3,4†},
Valerio Guarasi^{1†}, Paolo Soda^{1,2†}

¹ Unit of Artificial Intelligence and Computer Systems, Department of Engineering, Università Campus Bio-Medico di Roma, Rome, Italy.

²Department of Diagnostics and Intervention, Radiation Physics, Biomedical Engineering, Umeå University, Umeå, Sweden.

³Research Unit of Radiation Oncology, Department of Medicine and Surgery, Università Campus Bio-Medico di Roma, Rome, Italy.

⁴Operative Research Unit of Radiation Oncology, Fondazione Policlinico Universitario Campus Bio-Medico, Roma, Italy.

⁵Anatomical Pathology Operative Research Unit, Fondazione Policlinico Universitario Campus Bio-Medico, Rome, Italy.

⁶Research Unit of Anatomical Pathology, Department of Medicine and Surgery, Università Campus Bio-Medico di Roma, Rome, Italy.

⁷Department of Medicine and Surgery, Università Campus Bio-Medico di Roma, Roma, Italy.

⁸Operative Research Unit of Medical Oncology, Fondazione Policlinico Universitario Campus Bio-Medico, Roma, Italy.

⁹Operative Research Unit of Radiology and Interventional Radiology, Fondazione Policlinico Universitario Campus Bio-Medico, Roma, Italy.

¹⁰Department of Engineering ‘Enzo Ferrari’, University of Modena and Reggio Emilia, Modena, Italy.

¹¹University of Cassino and Southern Lazio, Cassino, Italy.

Contributing authors: filippo.ruffini@unicampus.it;

valerio.guarrasi@unicampus.it; pao.lo.soda@umu.se;

†F.R. and C.M.C. contributed equally to this work. S.R., V.G. and P.S. jointly supervised this work.

Abstract

Accurate survival prediction in Non-Small Cell Lung Cancer (NSCLC) requires the integration of heterogeneous clinical, radiological, and histopathological information. While Multimodal Deep Learning (MDL) offers a promises for precision prognosis and survival prediction, its clinical applicability is severely limited by small cohort sizes and the presence of missing modalities, often forcing complete-case filtering or aggressive imputation. In this work, we present a missing-aware multimodal survival framework that integrates Computed Tomography (CT), Whole-Slide Histopathology (WSI) Images, and structured clinical variables for overall survival modeling in unresectable stage II–III NSCLC. By leveraging Foundation Models (FM) for modality-specific feature extraction and a missing-aware encoding strategy, the proposed approach enables intermediate multimodal fusion under naturally incomplete modality profiles. The proposed architecture is resilient to missing modalities by design, allowing the model to utilize all available data without being forced to drop patients during training or inference. Experimental results demonstrate that intermediate fusion consistently outperforms unimodal baselines as well as early and late fusion strategies, with the strongest performance achieved by the fusion of WSI and clinical modalities (**73.30** C-index). Further analyses of modality importance reveal an adaptive behavior in which less informative modalities, i.e., CT modality, are automatically down-weighted and contribute less to the final survival prediction. Beyond predictive performance, the learned risk scores enable clinically meaningful stratification of disease progression and metastatic risk, supported by statistically significant log-rank tests, underscoring the clinical relevance of the proposed missing-aware multimodal framework. To promote reproducibility and accelerate future research on missing-aware multimodal oncology modeling, we will publicly release the curated dataset.

Keywords: Missing Data, Survival Analysis, Foundation Models, Oncology
Prognosis, eXplainable Artificial Intelligence, Multimodal Learning

1 Introduction

Lung cancer persists as a leading cause of cancer-related mortality worldwide, with Non-Small Cell Lung Cancer (NSCLC) accounting for approximately 85% of all diagnosed cases [Huang et al. \(2025\)](#). Although the advent of targeted therapy and immunotherapy has markedly reshaped the therapeutic landscape of NSCLC [Vincent et al. \(2025\)](#), these advances have also intensified the need to accurately identify patients with different levels of risk, as treatment efficacy varies widely across individuals. Accurate risk estimation is supportive to critical therapeutic choices [Yuan](#)

et al. (2025), such as selecting the appropriate treatment modality, adjusting treatment intensity, and defining follow-up strategies, according to each patient's expected clinical trajectory. Nonetheless, prognostic risk in NSCLC arises from a complex interplay of biological and clinical factors that no single biomarker or imaging modality can fully capture, making a comprehensive understanding of patient prognosis dependent on information drawn from complementary sources [Guarrasi et al. \(2025b, 2024\)](#).

Histopathology, radiology, genomic information, and Electronic Health Records (EHR) provide multi-scale views of tumor morphology, molecular profile, and patient health status [Captier et al. \(2025\)](#). Histopathology, obtained from digital Whole Slide Images (WSI), remains the diagnostic gold standard, offering high-resolution insight into microscopic morphology. Beyond diagnosis, it holds significant prognostic value by revealing the tumor microenvironment and immune infiltration patterns, which are key determinants of survival. Yet, because biopsies are invasive and focal, they often fail to capture the full spatial heterogeneity of the tumor [Guedes et al. \(2025\)](#). Radiological imaging, primarily Computed Tomography (CT), provides a macroscopic and non-invasive view of the entire tumor burden. However, while it overcomes the sampling bias of biopsies, radiological assessment remains susceptible to subjective qualitative interpretation and provides limited prognostic signal when used in isolation to predict disease outcome [Paverd et al. \(2024\)](#). Genomic information, derived from molecular sequencing, characterizes the tumor's underlying genetic landscape. By identifying specific oncogenic drivers and mutations, it offers critical predictive biomarkers for targeted therapy, although it does not reflect the physical characterization of the tumor. Finally, EHRs aggregate the essential patients' clinical context, ranging from physiological parameters and comorbidities to treatment history, into structured tabular data. These clinical variables are indispensable for linking biological findings to actual survival outcomes and monitoring disease progression [Lobato-Delgado et al. \(2022\); Peng et al. \(2019\)](#). To enable robust modeling and harmonization across patients, a common practice is to process EHR data, aggregating key physiological variables, comorbidities, and treatment history, uniforming them into structured tabular formats.

In this intricate tangle of multi-source information, Artificial Intelligence (AI) research in medicine has increasingly converged around the paradigm of Multimodal Deep Learning (MDL). Unlike traditional Deep Learning (DL) approaches that process modalities in isolation, MDL is designed to construct unified patient representations by fusing heterogeneous data sources. In the context of NSCLC, MDL aims to capture latent non-linear relationships that extend across biological scales, bridging the gap between the microscopic tissue architecture of WSI, the macroscopic tumor morphology of CT, and the systemic clinical reality. Such an interaction between diverse modalities can be adopted to for next generation of personalized cancer care [Niu et al. \(2025\)](#).

The integration of these diverse streams is pivotal to predict prognostic outcomes, as it enables clinicians to move beyond a static snapshot of disease status and more accurately anticipate disease progression and patient outcomes. To translate this multimodal perspective into actionable predictions, prognosis in oncology can be formulated as an **Overall Survival (OS)** modeling task [Machin et al. \(2006\)](#), the standard

quantitative framework for estimating patient outcomes [Soenksen et al. \(2022\)](#). Unlike binary classifiers, which collapse prognosis into a static mortality label, OS modeling uses time-to-event analysis to estimate survival probabilities over time. Handling of censored observations, i.e., patients who are lost to follow-up or who remain event-free at analysis, is a key strength of this formulation, thus ensuring that all available longitudinal information contributes to estimate the survival prediction [Caruso et al. \(2024a\)](#).

From these survival functions, OS models generate continuous, patient-specific risk scores that quantify individual prognosis. These scores are then used to stratify patients into clinically meaningful risk groups, typically via median or quantile thresholds, to distinguish individuals with aggressive disease trajectories from those who are likely to experience more indolent courses [Lee et al. \(2025\)](#). Such stratification is central to precision oncology, informing decisions on therapeutic intensity, surveillance frequency, and eligibility for targeted or experimental treatments.

Unlike binary classifiers, which collapse prognosis into a static mortality label, OS modeling uses time-to-event analysis to estimate the survival function $S(t|x)$. This function represents the probability that a specific patient with clinical features x will survive beyond any given time t . The ability of these models to handle of censored observations, i.e., patients who are lost to follow-up or who remain event-free at analysis, is the key strength of this formulation, ensuring that all available longitudinal information contributes to the estimation of the curve [Caruso et al. \(2024a\)](#). From these estimated survival probabilities, the models derive continuous, patient-specific risk scores (often summarizing the cumulative hazard or expected median survival). The resulting scores are then used to stratify patients into clinically meaningful risk groups, typically via median or quantile thresholds, to distinguish patients with aggressive disease trajectories from those likely to experience more indolent courses [Lee et al. \(2025\)](#). Such stratification is central to precision oncology, informing decisions on therapeutic intensity, surveillance frequency, and eligibility for targeted or experimental treatments. Historically, survival modeling has been largely explored by Machine-Learning (ML) approaches, most notably the Cox Proportional Hazards (CPH) model and Random Survival Forests (RSF) [Graf et al. \(2025\)](#). These models perform well when applied to structured, low-dimensional clinical variables; however, they are not designed to operate directly on high-dimensional data such as CT volumes or WSI. As a result, MDL provides a robust path toward more accurate and clinically actionable survival estimation in NSCLC [Yang et al. \(2025\)](#); [Wu et al. \(2025\)](#); [Oh et al. \(2023\)](#); [Lee et al. \(2025\)](#). Despite that, the clinical translation of Multimodal Deep Learning (MDL) frameworks remains fundamentally constrained by the limited availability of comprehensive multimodal oncology datasets. In real-world oncological settings, two pervasive structural limitations systematically hinder the robustness and generalizability of MDL models: restricted cohort sizes and the occurrence of partially missing or fragmented modalities [Guarrasi et al. \(2024\)](#); [Yang et al. \(2024\)](#). First, the inherent scarcity of labeled data and heterogeneity of medical datasets create a heavy risk of overfitting, particularly when attempting to train deep encoders from scratch on high-dimensional inputs. To address this bottleneck, the field has

increasingly adopted Foundation Models (FMs) to extract high-level and semantically rich representations for each input modality. The core idea is to leverage their massive pre-training, that would help them acquire a generalist representation of the data distribution [Bommasani \(2021\)](#). In healthcare, FMs have demonstrated remarkable robustness in high-variance clinical settings [Zhang and Metaxas \(2023\)](#); [Li et al. \(2024\)](#). While their utility as feature extractors is well-validated for diagnostic tasks across both CT and WSI images [Lu et al. \(2023\)](#); [Ding et al. \(2025\)](#); [Blankemeier et al. \(2024\)](#); [Xu et al. \(2024\)](#), their application to prognosis prediction remains significantly underexplored [Ruffini et al. \(2025\)](#). Unlike static diagnosis, deploying these generalist representations for survival analysis requires validating whether they capture the temporal and prognostic signals hidden within the tumor.

Second, medical data are inherently incomplete. Missingness arises both at the level of individual variables and entire diagnostic modalities, reflecting the realities of clinical workflows. Tabular clinical data may be incomplete due to non-response, human error during data entry, attrition in longitudinal records, data corruption, or systematic omissions linked to specific clinical pathways. Likewise, full imaging modalities may be absent: CT scans may not be acquired for patients treated in external institutions, histopathology slides may be unavailable when biopsies are not collected in the same institution as the or technically unsuccessful. As a result, real-world cohorts rarely contain a full, uniform set of measurements for every patient.

On these grounds, in this work we introduce a novel and resilient approach of MDL that predicts the OS of NSCLC patients. It can be trained on limited data, even in presence of missing data or missing modality. Similarly, its resilience to operate in real-world cases is further enhanced by the chance to run inference on new samples when a portion of the data is missing.

Indeed, To overcome the challenges of training high-capacity vision encoders on small clinical cohorts, stage (i) unimodal feature extraction using pretrained FMs for CT and WSI, which map raw imaging data into generalist features; (ii) missing-aware representation learning, in which each modality is elaborated through a transformer-based architecture customized with an adaptive masking mechanism that enables the network to ignore unavailable inputs; and (iii) an intermediate multimodal fusion strategy for survival prediction, where the modality-specific latent representations are concatenated and fused within an *Oblivious Differentiable Decision Tree* (ODST) head [Langley and Sage \(1994\)](#), explicitly modeling cross-modal interactions and producing a continuous, patient-specific hazard estimate for overall survival. Given the proposed missing-aware architecture, we conducted a modality-importance analysis by systematically varying the degree of missingness in tabular, CT, and WSI inputs and monitoring the corresponding changes in OS prediction at test time. This missingness-driven analysis provides an interpretable view of modality relevance, revealing complementary and redundant information across data streams and offering clinically actionable insights on model trustworthiness. Finally, to promote transparency and reproducibility, we have made the complete dataset from this study publicly available. This release is intended to enable independent validation of our findings and to accelerate future research into multimodal modeling within oncology.

2 Results

This section presents the results of the proposed three-stage, missing-aware multi-modal learning framework. We report performance across unimodal, bimodal, and trimodal configurations, with a focus on robustness under incomplete patient profiles.

2.1 Cohort Characteristics

Table 1 Cohort characteristics stratified by survival status.

Characteristic	Overall (n=179)	Non-Survivor (n=99)	Survivor (n=80)	P-value
Age (years)	69.8 \pm 12.0	70.0 \pm 12.5	69.6 \pm 11.3	0.820
Sex				0.039*
Female	50 (27.93%)	21 (21.2%)	29 (36.2%)	
Male	129 (72.07%)	78 (78.8%)	51 (63.7%)	
Weight (kg)	70.3 \pm 13.9	72.4 \pm 14.0	68.1 \pm 13.5	0.160
Height (cm)	168.3 \pm 8.9	169.8 \pm 9.1	166.7 \pm 8.5	0.112
NRS	0.3 \pm 1.3	0.4 \pm 1.5	0.2 \pm 1.0	0.419
Smoking habitus				0.521
Ex-smoker	43 (53.75%)	23 (56.1%)	20 (51.3%)	
Smoker	28 (35.00%)	15 (36.6%)	13 (33.3%)	
Non-smoker	9 (11.25%)	3 (7.3%)	6 (15.4%)	
Cigarettes/day	22.4 \pm 18.7	23.8 \pm 19.5	21.0 \pm 18.2	0.547
Stage at diagnosis				0.540
IIA	2 (1.12%)	1 (1.0%)	1 (1.2%)	
IIB	5 (2.79%)	3 (3.0%)	2 (2.5%)	
IIIA	84 (46.93%)	48 (48.5%)	36 (45.0%)	
IIIB	71 (39.66%)	41 (41.4%)	30 (37.5%)	
IIIC	17 (9.50%)	6 (6.1%)	11 (13.8%)	
Histology				0.331
Adenocarcinoma	90 (50.28%)	48 (48.5%)	42 (52.5%)	
Squamous carcinoma	80 (44.69%)	44 (44.4%)	36 (45.0%)	
NOS	5 (2.79%)	3 (3.0%)	2 (2.5%)	
Other	4 (2.23%)	4 (4.0%)	0 (0.0%)	
Comorbidity 1				0.479
Vascular	48 (64.00%)	25 (65.8%)	23 (62.2%)	
Metabolic	12 (16.00%)	4 (10.5%)	8 (21.6%)	
Renal	2 (2.67%)	2 (5.3%)	0 (0.0%)	
Other	11 (14.67%)	6 (15.8%)	5 (13.5%)	
Pulmonary	2 (2.67%)	1 (2.6%)	1 (2.7%)	
Comorbidity 2				0.756
Vascular	6 (11.76%)	2 (7.7%)	4 (16.0%)	
Metabolic	26 (50.98%)	15 (57.7%)	11 (44.0%)	
Renal	3 (5.88%)	2 (7.7%)	1 (4.0%)	
Pulmonary	5 (9.80%)	2 (7.7%)	3 (12.0%)	
Other	11 (21.57%)	5 (19.2%)	6 (24.0%)	
Comorbidity 3				0.253
Vascular	1 (6.67%)	0 (0.0%)	1 (12.5%)	
Metabolic	1 (6.67%)	1 (14.3%)	0 (0.0%)	
Renal	2 (13.33%)	0 (0.0%)	2 (25.0%)	
Other	10 (66.67%)	6 (85.7%)	4 (50.0%)	
Pulmonary	1 (6.67%)	0 (0.0%)	1 (12.5%)	
ECOG PS				0.101
0	60 (70.59%)	26 (60.5%)	34 (81.0%)	
1	23 (27.06%)	16 (37.2%)	7 (16.7%)	
2	2 (2.35%)	1 (2.3%)	1 (2.4%)	

Continuous variables are presented as mean \pm standard deviation, and categorical variables as n (%). P-values were calculated using one-way analysis of variance for continuous variables and chi-square test for categorical variables. RT *RadioTherapy*, Ch.T *ChemoTherapy*. Statistical significance is indicated as follows: $p < 0.05$ (*), $p < 0.005$ (**), and $p < 0.001$ (***)

Table 2 (Table 1 Continued) Cohort characteristics stratified by survival status.

Characteristic	Overall (n=179)	Non-Survivor (n=99)	Survivor (n=80)	P-value
EGFR mutation				0.033*
Negative	41 (87.23%)	23 (100.0%)	18 (75.0%)	
Positive	6 (12.77%)	0 (0.0%)	6 (25.0%)	
ALK rearrangement				0.233
Negative	45 (93.75%)	24 (100.0%)	21 (87.5%)	
Positive	3 (6.25%)	0 (0.0%)	3 (12.5%)	
MET alteration				1.000
Negative	4 (66.67%)	1 (100.0%)	3 (60.0%)	
Positive	2 (33.33%)	0 (0.0%)	2 (40.0%)	
PD-L1 (%)	0.2 ± 0.3	0.2 ± 0.3	0.2 ± 0.3	0.776
RT dose (Gy)	59.1 ± 8.9	58.3 ± 10.3	60.1 ± 6.8	0.176
Number of fractions	28.6 ± 5.3	27.9 ± 6.3	29.3 ± 3.8	0.211
RT Technique				< 0.001***
3DCRT	43 (30.28%)	32 (43.2%)	11 (16.2%)	
VMAT	80 (56.34%)	39 (52.7%)	41 (60.3%)	
Mixed	6 (4.23%)	2 (2.7%)	4 (5.9%)	
RA	13 (9.15%)	1 (1.4%)	12 (17.6%)	
Induction Ch.T				0.465
CC	13 (43.33%)	7 (50.0%)	6 (37.5%)	
gem	1 (3.33%)	0 (0.0%)	1 (6.2%)	
C	15 (50.00%)	6 (42.9%)	9 (56.2%)	
CC+gem	1 (3.33%)	1 (7.1%)	0 (0.0%)	
Concomitant Ch.T				0.351
CC	58 (44.96%)	31 (42.5%)	27 (48.2%)	
Gem.	13 (10.08%)	8 (11.0%)	5 (8.9%)	
C	8 (6.20%)	3 (4.1%)	5 (8.9%)	
CC+Gem	35 (27.13%)	22 (30.1%)	13 (23.2%)	
Al.	2 (1.55%)	0 (0.0%)	2 (3.6%)	
other	13 (10.08%)	9 (12.3%)	4 (7.1%)	
RT (days)	48.7 ± 12.2	48.3 ± 11.5	49.1 ± 13.0	0.695
Suspension days	2.9 ± 7.6	3.8 ± 9.9	2.0 ± 4.2	0.279
Adjuvant immunotherapy				0.010*
No	138 (77.09%)	84 (84.8%)	54 (67.5%)	
Yes	41 (22.91%)	15 (15.2%)	26 (32.5%)	
Esophageal toxicity				0.183
Grade 0	57 (67.86%)	31 (72.1%)	26 (63.4%)	
Grade >0	27 (32.14%)	12 (27.9%)	15 (36.6%)	
Pulmonary toxicity				0.250
Grade 0	75 (88.24%)	36 (83.7%)	39 (92.9%)	
Grade >0	10 (11.76%)	7 (16.3%)	3 (7.1%)	
Hemoglobin toxicity				0.276
Grade 0	76 (89.41%)	36 (83.7%)	40 (95.2%)	
Grade >0	9 (10.59%)	7 (16.3%)	2 (4.8%)	
Neutrophil toxicity				0.709
Grade 0	72 (84.71%)	37 (86.0%)	35 (83.3%)	
Grade >0	13 (15.29%)	6 (14.0%)	7 (16.7%)	
Platelet toxicity				0.440
Grade 0	68 (80.00%)	36 (83.7%)	32 (76.2%)	
Grade >0	17 (20.00%)	7 (16.3%)	10 (23.8%)	
PFS event				< 0.001***
censored	65 (36.31%)	21 (21.2%)	44 (55.0%)	
uncensored	114 (63.69%)	78 (78.8%)	36 (45.0%)	
DM event				< 0.001***
censored	88 (49.16%)	35 (35.4%)	53 (66.2%)	
uncensored	91 (50.84%)	64 (64.6%)	27 (33.8%)	

Continuous variables are presented as mean ± standard deviation, and categorical variables as n (%). P-values were calculated using one-way analysis of variance for continuous variables and chi-square test for categorical variables. RT RadioTherapy; Ch.T ChemoTherapy; PFS Progression Free Survival; DM Distant Metastasis. Statistical significance is indicated as follows: $p < 0.05$ (*), $p < 0.005$ (**), and $p < 0.001$ (***)�.

Our study is based on a retrospective cohort of 179 patients with unresectable Stage IIA, IIB, IIIA, IIIB and IIIC NSCLC treated with radical Chemo-Radiotherapy. Tables 1 and 2 report the results of a univariate analysis of baseline cohort characteristics in relation to overall survival. Patients are stratified into Survivors ($n = 80$) and Non-survivors ($n = 99$) according to their status at the last follow-up. The tables

summarize univariate relationshipt between clinical, demographic, histological, and treatment-related variables and survival groups.

Across demographic variables, the mean age of the cohort was 69.8 ± 12.0 years, with similar distributions in the Survivor (69.6 ± 11.3) and Non-survivor (70.0 ± 12.5) groups ($p = 0.820$). A significant difference was observed for sex ($p = 0.039$), with males representing 78/99 (78.8%) of non-survivors compared to 51/80 (63.7%) of survivors, indicating a statistically significant association between sex and worse survival outcomes. Stage at diagnosis was similarly distributed ($p = 0.540$), with stage IIIA observed in 48/99 non-survivors and 36/80 survivors, and Stage IIIB in 41/99 and 30/80 patients, respectively. Histological subtype stratification were comparable between the groups ($p = 0.331$), with majority of cases identified as adenocarcinoma (48/99 for non survivor compared to 42/80 for survivor) and squamous carcinoma (44/99 and 36/80). Similar patterns were observed for renal, pulmonary, and other comorbidity categories. For example, vascular comorbidities were reported in 25/38 (65.8%) non-survivors and 23/37 (62.2%) survivors ($p = 0.479$), and metabolic comorbidities in 15/26 (57.7%) and 11/25 (44.0%) patients ($p = 0.756$). Among molecular biomarkers, EGFR mutation status differed between groups ($p = 0.033$), with positive cases found exclusively among Survivors (7.5% compared to 0% in Non-survivors). This difference highlights the known favorable prognostic impact of EGFR mutations, likely attributable to the distinct biology of this subtype and the availability of effective targeted therapies [Lee et al. \(2013\)](#). Moreover, a highly significant variation was also observed in radiotherapy techniques ($p < 0.001$), reflecting the survival advantage associated with modern delivery methods. Survivors were more frequently treated with VMAT (60.3%), whereas usage of 3D-CRT was nearly three times higher in the non-survivor group (43.2% vs. 16.2%), suggesting an association between older conformal techniques and poorer prognostic outcomes.

The administration of adjuvant immunotherapy was significantly associated with improved survival ($p = 0.010$). Its higher prevalence among Survivors (32.5% vs. 15.2%) reflects the benefit of consolidation checkpoint inhibition in Stage III NSCLC, reinforcing that access to contemporary systemic therapy remains a major prognostic determinant in this setting [Spigel et al. \(2022\)](#).

However, a stark dichotomy emerged when analyzing the intermediate clinical endpoints, highlighting that mortality is fundamentally driven by the disease's trajectory rather than baseline demographics. *Progression-Free Survival (PFS)* events were strongly correlated with mortality ($p < 0.001^{***}$): the vast majority of non-survivors (78.8%) experienced a progression event compared to less than half of the survivors (45.0%). This pattern was further reinforced by the rates of *Distant Metastasis (DM)* ($p < 0.001^{***}$). Systemic failure was a hallmark of the non-survivor group, with 64.6% developing distant metastases versus only 33.8% in the survivor group. These findings confirm that while the two groups were demographically and clinically balanced at baseline, their outcomes were determined by the distinct biological aggressiveness of the tumor, manifesting as therapeutic resistance (PFS events) and systemic spread (DM). We examine in detail the impact of progression events on model performance in the following results sections. Finally, no statistically relevant differences were observed for the remaining baseline characteristics. Variables such as age ($p = 0.820$), TNM

stage ($p = 0.540$), histology ($p = 0.331$), and ECOG performance status ($p = 0.101$) were evenly distributed between survivors and non-survivors. While our primary endpoint is time-to-event, the survivor/non-survivor univariate analysis is included as an exploratory cohort characterization to provide an interpretable snapshot of baseline differences and verify that covariate trends are directionally consistent with the survival outcome.

2.2 Missing Modalities and Tabular Data Sparsity

The cohort of this study is characterized by significant data heterogeneity, presenting variable levels of missingness and feature sparsity. As illustrated in Figure 1, data availability is unevenly distributed across acquisition modalities and within the tabular clinical domain itself. At the modality level (Figure 1.a), WSI constitutes the primary bottleneck, being available for only 33.5% of patients ($n = 60$). By contrast, radiological imaging (CT) shows near-complete coverage, with only 2.8% of cases lacking a scan. Nevertheless, the intersection of modalities remains narrow: 22.9% of patients ($n = 41$) possess the full trimodal profile (CT + WSI + Tabular).

However, full modality-level availability in the Tabular modality does not imply that its constituent clinical features have been fully collected. Figure 1.b shows that the structured clinical data, despite being technically present for all patients, exhibits substantial internal sparsity. Several clinically relevant molecular biomarkers, such as EGFR, ALK, and MET mutation status, are absent in 73.7%, 73.2%, and 96.6% of patients, respectively. This missingness reflects a structural limitation of real-world clinical workflows, where molecular testing is not always performed and retrospective collection of these exams is challenging or even impossible.

Additional laboratory and histopathological descriptors (e.g., PD-L1 expression) exhibit comparable levels of incompleteness. Beyond genomic indicators, clinical information as comorbidities are often incompletely documented, leading to substantial under-reporting of cardiovascular, metabolic, and respiratory conditions. The combined effect of cross-modal and intra-modal sparsity has profound implications for learning. Conventional multimodal architectures often rely on a “complete-case” design, admitting only patients with a full set of modalities. Under this assumption, 77.1% of our cohort would be excluded (Figure 1a), disproportionately removing patients with incomplete diagnostic workups, typically those with aggressive disease trajectories, comorbidities, or limited access to comprehensive staging procedures. Such filtering should introduce substantial selection bias and undermine the clinical validity of downstream models. To overcome these issues, our approach is designed to handle both missing modalities and clinical features, allowing for the inclusion of the entire patient cohort without data imputation or exclusion.

2.3 Missing-Aware Multimodal Survival Modeling

To support multimodal survival prediction under realistic clinical missingness, we propose a three-stage framework that decouples: (Step 1) FM feature extraction process, (Step 2) missing-aware unimodal encoding, and (Step 3) an intermediate multimodal learning model. Figure 2 provides a schematic of the complete framework.

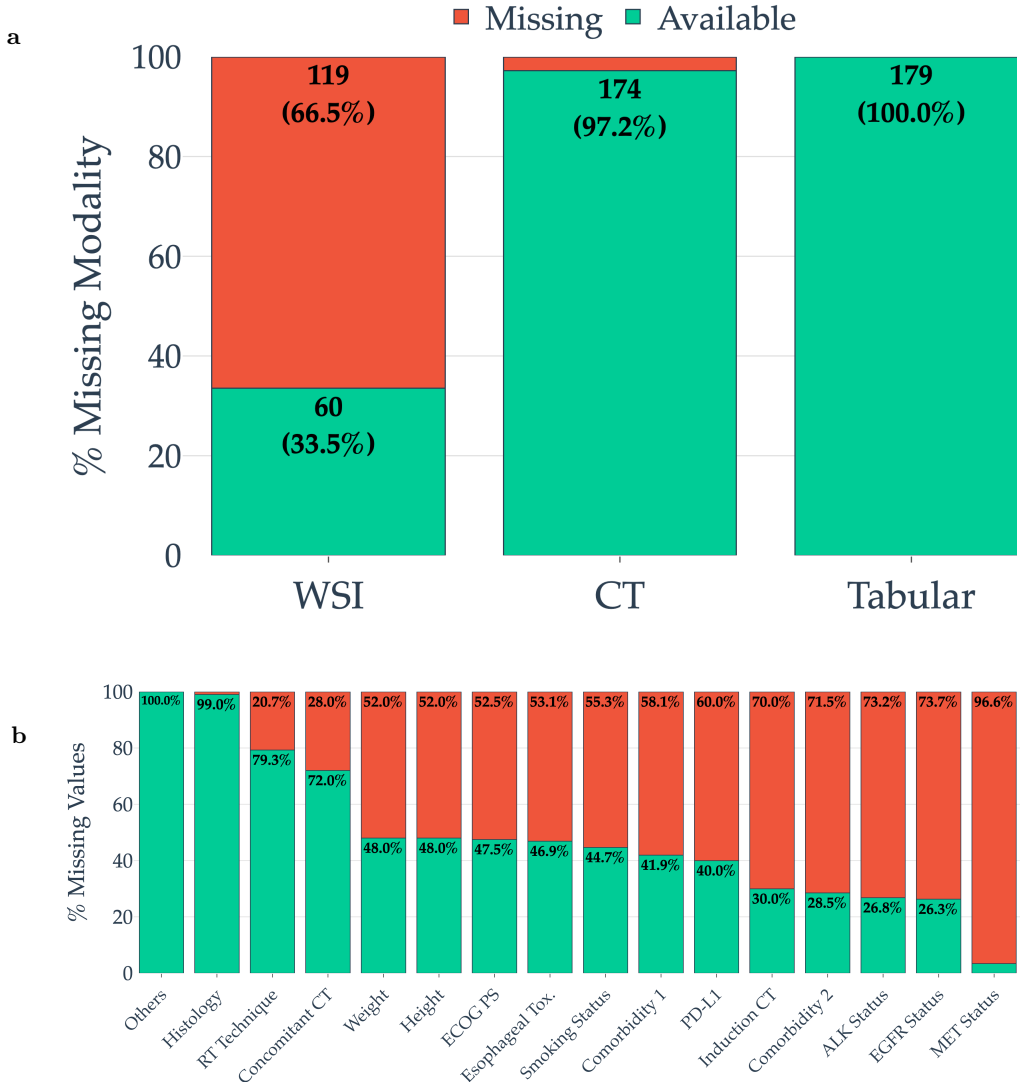


Fig. 1 Overview of modality availability and clinical data sparsity in the cohort. Panel a reports the availability of entire diagnostic modalities (WSI, CT and Tabular data) across the cohort. Panel b presents the percentage of missing values that characterize the Tabular modality, detailing missingness rates for each individual features.

Step 1 performs modality-specific pre-processing and feature extraction through functions $\Phi_i(\cdot)$, which map each raw input x_i to a fixed embedding x_i^* . In practice, Φ_1 denotes the Tabular pre-processing pipeline, Φ_2 corresponds to CT pre-processing and encoding, and Φ_3 implements the WSI processing flow (tissue segmentation, patch encoding, and slide-level aggregation). **Step 2** transforms each x_i^* through a modality-specific encoder $F_i(\cdot)$, which implements missing-aware tokenization and masked self-attention, yielding a latent representation h_i that is conditioned only on observed

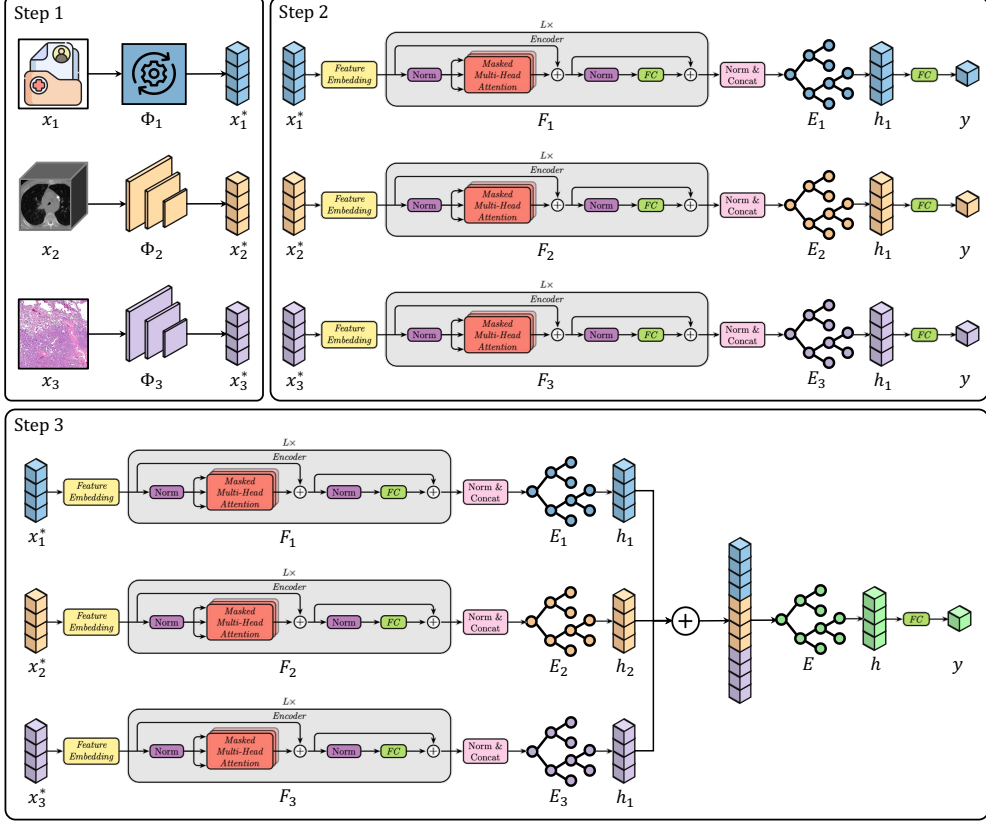


Fig. 2 Schematic overview of the proposed Multimodal Survival Framework. The architecture integrates three distinct clinical data streams: Pathology (WSI), Radiology (CT), and Tabular Clinical data. **Step 1: Preprocessing & Feature Extraction.** High level representations are extracted using domain-specific FMs. Whole Slide Images are processed via CLAM and encoded using the WSI patch extraction pipeline; volumetric CT scans are encoded using the Merlin 3D ViT encoder. **Step 2: Missing-Aware Encoding.** Each modality stream is processed by a dedicated NAIM+ODST encoder. This transformer-based encoder employs an adaptive masking mechanism to dynamically handle missing modalities without imputation. **Step 3: Intermediate Fusion & Prediction.** The diagram visualizes the fusion paradigms. In the proposed intermediate fusion, latent representations from the NAIM+ODST encoders are concatenated and fed into an ODST layer to predict the output patient-specific hazard function y .

inputs. Each h_i is then processed by an ODST block $E_i(\cdot)$, followed by a lightweight fully connected projection, to produce a unimodal risk estimate. **Step 3** implements the final intermediate fusion model, where the latent vectors h_i from all the modalities are concatenated (\oplus) into a unified representation h_m , which is then passed to a multimodal ODST module $E_m(\cdot)$ and a final fully connected layer to generate the multimodal survival risk prediction y . Overall, the figure emphasizes that missing modalities are handled structurally via masking within $F_i(\cdot)$, enabling the model to

operate on incomplete modality profiles without explicit modality imputation (full definitions are deferred to Section 5.1).

2.4 Prognostic Separability in FMs' Representation Spaces

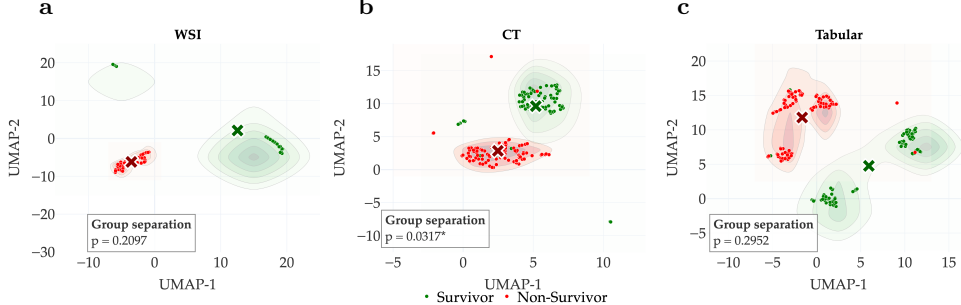


Fig. 3 2D UMAP projections derived from FM embeddings for: a) WSI, b) CT, and c) Tabular. Each plot displays the distribution of **Survivors** (green data points) and **Non-survivors** (red data points), including kernel density contours and class centroids. The annotation in each panel reports the p-value of the group separation test computed on the embedding space.

To enable robust unimodal representation learning under the constraints of a limited cohort size, we first extracted imaging-derived features using pretrained foundation models (FMs). Specifically, WSI representations are obtained by combining CLAM-based patch aggregation with MI-Zero vision encoders and the TITAN framework Ding et al. (2025); Lu et al. (2023, 2021), which outputs 768 features. For CT volumes, the representation are obtained using the 3D ViT-based backbone from Merlin Blankemeier et al. (2024), which outputs for each CT a representation token with 2048 features. By leveraging large-scale pretraining, these encoders yield highly generalist representation that could help reduce overfitting (implementation details are reported in Section 5). For completeness, tabular variables were included after imputing missing values using median imputation for continuous features and k -nearest neighbors for categorical features.

Using these unimodal embeddings, we then conducted an exploratory representation analysis to assess whether each modality encodes relevant prognosis signals. Figure 3 shows two-dimensional UMAP projections of the unimodal representation spaces. Importantly, this analysis is not intended to reflect the time-to-event survival modeling task addressed in this work, but rather to provide a preliminary, mortality-based assessment of prognostic signal. Consistent with the cohort characterization in Section 2.9, patients are stratified into *Survivors* and *Non-Survivors*, mirroring a uni-variate analysis designed to probe the discriminative capacity of each modality in isolation.

WSI embeddings in Fig. 3.a reveal locally coherent substructures, likely reflecting histological tissue organization, without achieving statistically relevant outcome-level separation ($p = 0.2097$). The overlap suggests that, although meaningful morphological patterns are encoded, the unsupervised histopathological representations obtained

in our framework alone do not linearly discriminate prognostic groups. This limitation is plausibly attributable to high intra-class heterogeneity and the relatively small number of available WSIs, which constrains reliable manifold estimation. In contrast, CT embeddings in Fig. 3.b exhibit a clear structural separation between *Survivors* (green) and *Non-Survivors* (red), a pattern supported by a statistically significant group-separation test ($p = 0.0317$). This indicates that CT-derived representations capture a strong macroscopic prognostic signal. Similarly, the Tabular modality in Figure 3.c displays high variance and no discernible boundary between outcome groups ($p = 0.2952$). The lack of separability in this structured feature space underscores the difficulty of stratifying patients using clinical variables alone.

Taken together, these observations motivate a multimodal integration strategy, as none of the three data streams, when considered in isolation, provides a fully reliable prognostic separation, yet they capture complementary signals that may become synergistic when jointly modeled. In the following section, we move beyond exploratory mortality-based analyses and quantitatively evaluate the predictive performance of each unimodal representation on the full survival modeling task.

2.5 FMs enable Unimodal Prognostic Modeling

Table 3 Unified unimodal performance across WSI, CT and Tabular modalities. ML: classical ML models (CPH, RSF, SGB). DL: DL architectures (NN, NAIM, NAIM+ODST). Mean \pm standard error of the mean (SEM, 5-fold CV). The best-performing model for each modality is highlighted in **bold**.

Modality	Model	Type	C-index	Uno C-index	td-AUC
WSI	CPH	ML	49.71 \pm 2.27	43.79 \pm 3.29	50.62 \pm 2.26
	RSF	ML	65.47 \pm 1.15	62.51 \pm 1.67	62.68 \pm 2.69
	SGB	ML	55.57 \pm 4.16	52.55 \pm 5.62	53.95 \pm 7.61
	NN	DL	44.78 \pm 4.77	45.21 \pm 5.49	51.64 \pm 5.95
	NAIM	DL	53.62 \pm 4.83	52.55 \pm 6.09	58.67 \pm 7.18
	NAIM+ODST	DL	60.91 \pm 6.01	56.28 \pm 2.69	65.33 \pm 4.64
CT	CPH	ML	52.84 \pm 2.53	53.51 \pm 2.39	58.14 \pm 2.34
	RSF	ML	51.21 \pm 2.74	53.33 \pm 1.71	54.65 \pm 3.72
	SGB	ML	52.35 \pm 1.70	51.55 \pm 2.37	54.39 \pm 3.57
	NN	DL	56.98 \pm 4.44	57.39 \pm 4.64	63.63 \pm 6.11
	NAIM	DL	53.69 \pm 5.25	54.57 \pm 2.06	54.23 \pm 3.18
	NAIM+ODST	DL	62.20 \pm 4.12	63.17 \pm 3.06	64.69 \pm 3.87
Tabular	CPH	ML	59.72 \pm 4.78	57.75 \pm 3.39	65.05 \pm 7.39
	RSF	ML	67.47 \pm 3.61	62.39 \pm 2.20	75.28 \pm 3.84
	SGB	ML	57.58 \pm 4.12	56.72 \pm 3.95	60.75 \pm 5.36
	NN	DL	59.02 \pm 3.92	55.94 \pm 2.27	66.48 \pm 5.82
	NAIM	DL	64.14 \pm 3.66	61.75 \pm 3.33	69.68 \pm 4.60
	NAIM+ODST	DL	66.00 \pm 2.26	63.56 \pm 4.35	72.73 \pm 5.57

To quantitatively assess the prognostic value of each unimodal representation, we evaluated their performance on the time-to-event OS task using established machine-learning methods for time-to-event analysis. Specifically, we considered Cox Proportional Hazards (CPH), Random Survival Forests (RSF), and Survival Gradient Boosting (SGB), which represent complementary survival modeling paradigms and are widely used as clinical baselines. /bl Regarding the Tabular modality, the three survival models differ in their treatment of missing values. Cox Proportional Hazards (CPH) and Random Survival Forests (RSF) can handle missing entries during model fitting and are therefore applied directly to the available clinical features. In contrast, Survival Gradient Boosting (SGB) requires complete inputs; accordingly, missing values were handled via K -Nearest Neighbor (KNN) imputation prior to training. For imaging-derived modalities (CT and WSI), patients lacking the corresponding modality were excluded from the unimodal analysis of that specific data stream. To ensure comparability across experiments, the same five-fold cross-validation splits were preserved across all unimodal evaluations, irrespective of modality availability.

In addition to classical ML baselines, we evaluated three (DL) architectures with testing different modeling capabilities. We first considered a transformer-based model inspired by the Not-Another-Imputation-Method (NAIM) [Caruso et al. \(2024b\)](#), which explicitly addresses missing values through masked self-attention. In the following, we refer to this architecture as NAIM. Building on this formulation, we evaluated two variants to isolate the contribution of different architectural components. The first variant is a Neural Network (NN) baseline that adopts the same continuous and categorical embedding scheme as NAIM but removes the transformer-based encoder, replacing it with a standard multi-layer perceptron (MLP). Unlike NAIM, this architecture does not handle missing values; therefore, missing features were imputed using KNN strategy prior to training. This configuration is specifically intended to assess the robustness conferred by NAIM’s missing-aware attention mechanism, by providing a direct comparison against an otherwise comparable model that relies on explicit imputation. Finally, we considered NAIM+ODST, which retains the NAIM model defined before but replaces the survival head with an Oblivious Differentiable Decision Tree (ODST) [Langley and Sage \(1994\)](#) layer. This extension was explored to search more advanced non-linear elaboration of the learned representations, with the objective to capture higher-order feature interactions relevant for survival prediction.

Table 3 reports all the experiments conducted in 5-fold cross validation, using Concordance index (C-ix), Uno Concordance index (Uno) and averaged time dependent Area Under the Curve (td-AUC). For WSI-derived features, the high dimensionality of the FM embeddings posed a significant challenge. While RSF maintained robustness with the highest C-index (65.47) and Uno score (62.51), NN struggled to generalize, yielding poor results across the board (Uno 45.21, td-AUC 51.64). However, the NAIM+ODST framework successfully bridged this gap. Although its Uno score (56.28) was lower than RSF, it achieved the highest td-AUC for the modality (65.33), surpassing RSF (62.68). This indicates that while RSF was better at global ranking, NAIM+ODST was highly effective at distinguishing patient outcomes at specific time points.

For CT-derived features, classical models showed closely aligned performance across all metrics. CPH achieved a C-ix of 52.84, with similar results for Uno (53.51) and td-AUC (58.14). RSF and SGB performed comparably, with RSF recording an Uno of 53.33 and SGB at 51.55. Among DL methods, the NN showed decent discrimination with a td-AUC of 63.63, though its ranking ability remained lower (Uno 57.39). The NAIM encoder alone did not show significant gains (Uno 54.57, td-AUC 54.23). However, the NAIM+ODST model emerged as the clear leader for this modality, achieving the highest scores across all three metrics: a C-ix of 62.20, an Uno of 63.17, and a td-AUC of 64.69, demonstrating superior stability in handling radiological features.

Within the Tabular modality, classical machine learning baselines demonstrated varied efficacy. RSF achieved the highest performance among traditional methods with a C-index of 67.47 and td-AUC of 75.28, significantly outperforming both CPH (td-AUC, 65.05) and SGB (td-AUC, 60.75). In the DL landscape, the proposed NAIM+ODST architecture emerged as the superior model. NAIM+ODST reached a C-index of 66.00 and achieved the highest Uno score in the tabular category (63.56), slightly surpassing RSF (62.39). While its td-AUC of 72.73 was lower than RSF, it represented a marked improvement over the standard NN (td-AUC 66.48) and a consistent gain over the standalone NAIM encoder (td-AUC, 69.68).

Based on this consistent performance across disparate modalities, NAIM+ODST was selected as the primary unimodal DL encoder for this study. This model serves as the unified backbone for mapping both structured clinical features and high-dimensional imaging representations (CT and WSI) into a shared prognostic space.

2.6 Intermediate fusion strategies maximize multimodal synergy

Building on the unimodal baselines presented in the previous section, Table 4 summarizes the performance of multimodal survival models under different fusion paradigms. The first block of the table reports the best-performing ML and DL models for each unimodal setting (WSI, CT, and Tabular), while the subsequent blocks compare multimodal architectures based on early, late, and intermediate fusion strategies [Teoh et al. \(2024\)](#). A detailed description of the model architectures and training procedures is provided in Section 5. Early fusion integrates information at the feature level by concatenating the latent representations extracted independently from each available modality. In this configuration, unimodal embeddings produced by pretrained NAIM+ODST encoders are concatenated prior to survival modeling and processed by a shared ODST followed by a fully connected (FC) layer. Since unimodal encoders are frozen, this setting, denoted as ConcatODST*, evaluates the representational complementarity of the modalities without joint optimization.

Intermediate fusion, denoted as ConcatODST, adopts the same architectural backbone but enables end-to-end optimization of the fusion module. Here, modality-specific representations are still concatenated; however, the ODST-based fusion head is trained jointly with the downstream survival objective, allowing the model to learn cross-modal interactions while preserving a structured decision process.

Modalities	Model	C-ix	Uno	td-AUC
Unimodal				
WSI	RSF (best ML)	65.47 ± 1.15	62.68 ± 2.69	62.51 ± 1.67
	NAIM+ODST	60.91 ± 6.01	56.28 ± 2.69	65.33 ± 4.64
CT	CPH (best ML)	52.84 ± 2.53	58.14 ± 2.34	53.51 ± 2.39
	NAIM+ODST	62.20 ± 4.12	63.17 ± 3.06	64.69 ± 3.87
Tabular	RSF (best ML)	67.47 ± 3.61	75.28 ± 3.84	62.39 ± 2.20
	NAIM+ODST	66.00 ± 2.26	63.56 ± 4.35	72.73 ± 5.57
Early Fusion (ConcatODST*)				
WSI+CT+Tabular	ConcatODST*	66.56 ± 4.42	63.87 ± 4.80	69.58 ± 6.92
WSI+CT	ConcatODST*	66.10 ± 2.39	64.30 ± 2.09	66.29 ± 1.65
WSI+Tabular	ConcatODST*	<u>70.63 ± 1.41</u>	66.77 ± 2.56	<u>75.34 ± 2.64</u>
CT+Tabular	ConcatODST*	65.69 ± 4.98	63.57 ± 4.24	71.88 ± 6.54
Late Fusion (NAIM+ODSTⁿ)				
WSI+CT+Tabular	NAIM+ODST ³	66.51 ± 4.07	62.97 ± 3.53	69.52 ± 4.52
WSI+CT	NAIM+ODST ²	66.47 ± 1.88	63.46 ± 2.64	72.84 ± 1.57
WSI+Tabular	NAIM+ODST ²	67.44 ± 3.08	67.19 ± 3.08	70.35 ± 4.07
CT+Tabular	NAIM+ODST ²	60.12 ± 2.42	56.61 ± 1.07	66.52 ± 2.59
Intermediate Fusion (ConcatODST)				
WSI+CT+Tabular	ConcatODST	68.77 ± 2.98	65.68 ± 3.49	70.88 ± 3.04
WSI+CT	ConcatODST	61.62 ± 2.87	59.30 ± 2.79	60.46 ± 3.60
WSI+Tabular	ConcatODST	73.30 ± 3.23	<u>70.04 ± 4.22</u>	78.68 ± 4.58
CT+Tabular	ConcatODST	65.24 ± 2.95	61.58 ± 1.99	71.56 ± 3.97

Table 4 Unified performance table including C-index (C-ix), Uno’s C-index (Uno), and averaged time-dependent AUC (td-AUC). Reported values are mean \pm standard error of the mean (SEM, 5-fold CV). For all experiments, evaluation was performed under the natural missingness patterns observed at test time (WSI 64%, CT 5%, and Tabular 0%). Unimodal baselines include the best ML models and deep-learning architectures in the unimodal settings, while multimodal results are reported for Early, Late, and Intermediate fusion strategies. The symbol * in Early Fusion (ConcatODST*) denotes feature-level concatenation of unimodal representations prior to survival modeling. The best-performing model for each metric is highlighted in **bold**, the second-best is underlined.

In contrast, late fusion combines modalities at the decision level rather than in the latent space. In this setting, separate unimodal NAIM+ODST models are trained independently for each modality, and their risk scores are subsequently aggregated to produce a final prediction. We indicate the late fusion approach by NAIM+ODSTⁿ,

where n represents the number of unimodal model involved to compute the final score. This strategy explicitly avoids feature-level interaction, serving as a strong baseline to assess whether multimodal gains arise from true cross-modal representation learning or from ensemble effects alone.

Among early fusion (ConcatODST*) modalities combinations, the *WSI+Tabular* configuration yields a consistent improvement over both contributing unimodal models, including the WSI ML baseline (RSF, 65.47 ± 1.15) and the tabular unimodal baseline (RSF, 67.47 ± 3.61), as well as their corresponding NAIM+ODST DL counterparts (60.91 ± 6.01 for WSI and 66.00 ± 2.26 for Tabular). Improvements are observed across all evaluated metrics, with the exception of the Uno C-index, where the tabular RSF baseline achieves the highest performance among all the configuration tested (75.283.84), multimodal fusion strategies included. This behavior is likely attributable to the robustness of tree-based ensemble methods to censoring patterns and their strong calibration in structured clinical feature spaces, which can be particularly advantageous for IPCW-based discrimination measures such as the Uno C-index [Hanika and Hirth \(2023\)](#). The *CT+Tabular* early fusion configuration reaches a C-index of 65.694.98, outperforming the best CT unimodal model (NAIM+ODST, 62.204.12) but inferior to the Tabular ML baseline (RSF, 67.47). Notably, *CT+Tabular* achieves a td-AUC of 71.886.54, higher than CT-only ML and DL best models and inferior only to *WSI+Tabular* early configuration, suggesting that clinical variables help compensate for the weaker discriminative power of CT features in isolation. The *WSI+CT* early fusion configuration yields a C-index of 66.102.39, superior to both the C-index obtained with WSI NAIM+ODST model (60.916.01) and slightly better the WSI RSF model (65.471.15). This indicates that CT information stabilizes the prognostic signal extracted from WSI, acting as a form of regularizer even under conditions of substantial pathology missingness (64%). Lastly, the trimodal early fusion model reaches a C-index of 66.562.39, outperforming all three unimodal NAIM+ODST baselines. The model obtained a competitive value of td-AUC around 69.586.92, highlighting the value of combining CT, WSI and Tabular modalities. However, the trimodal configuration does not surpass the bimodal WSI+Tabular configuration. We hypothesize that this behavior arises from the inclusion of the radiological modality, which may introduce additional variability that is not consistently informative for this cohort, thereby diluting the stronger complementary signal captured by WSI and Tabular modalities. Indeed, while CT provides macroscopic context, the features extracted appear less discriminative for survival in this specific cohort compared to the dense, biological signal of WSI and the structured context of clinical variables. Consequently, the addition of CT features to the WSI+Tabular pairing may reduce the prognostic signal rather than enhancing it.

We next examine the performance of late fusion, in which predictions from independently trained unimodal models are combined at the decision level. In the *CT+Tabular* configuration, late fusion yields a C-index of 60.122.42, markedly lower than both early (65.694.98) and intermediate (65.242.95) fusion strategies. This performance degradation highlights the limitations of unweighted decision-level aggregation, which does not account for disparities in predictive strength across modalities. Consequently, if one of the branches provides less informative or noisier predictions, this can reduce

the strength of the stronger clinical signal, leading to reduced performance. In contrast, intermediate architecture ConcatODST allow the model to learn non-linear interactions, effectively using clinical variables to gate or contextualize the radiological features before the final prediction is formed. Similarly, for the high-performing *WSI+Tabular* configuration, late fusion (67.443.08) C-index metric values fail to reach the results of early (70.631.41) or intermediate fusion (73.303.23). This underscores that the complementarity between histopathology and clinical data is not merely additive but synergistic, requiring a shared latent space to fully exploit the interaction between microscopic tumor biology and systemic patient health.

Intermediate fusion achieves the strongest overall performance across this study, consistently outperforming both unimodal baselines and their corresponding early and late fusion configurations. Performance improvements are observed across all previously discussed settings, with the *WSI+Tabular* configuration obtaining the second-highest Uno C-index among all evaluated models. The trimodal intermediate configuration achieved a C-index of 68.772.98, improving on the trimodal early fusion model (66.564.42) and outperforming all three unimodal NAIM+ODST branches. The td-AUC value obtained (70.883.04) is also larger than the early fusion trimodal result and inferior only to the *WSI+Tabular*, validating that end-to-end fine-tuning is essential for aligning the feature spaces in this trimodal configuration. Compared with ML baselines, trimodal intermediate fusion remains markedly superior respect the best unimodal baselines: CT CPH (52.842.53), WSI RSF model (65.471.15), and the Tabular RSF model (67.473.61). Nevertheless, the *WSI+Tabular* intermediate fusion model remains the top-performing configuration (C-index, 73.303.23). This suggests that for this cohort, the synergy between the microscopic tissue architecture (WSI) and the systemic patient status (Tabular) captures the most salient prognostic information. The inclusion of clinical variables provides a stable and low-variance source of information that constrains the representation learned from histological features. This interaction reduces the impact of histology-specific variability and yields a more focused and discriminative latent representation. As a result, the bimodal WSI+Tabular model achieves greater robustness than the trimodal configuration, where the additional radiological modality introduces variability that is not consistently informative for this cohort.

The *CT+Tabular* intermediate fusion model reaches a C-index of 65.242.95, similar to its early fusion counterpart (65.694.98). While the early fusion variant already exceeded the CT unimodal models, intermediate fusion results show a lower standard error, suggesting a smoothing effect when CT and clinical variables are optimized jointly. By contrast, *WSI+CT* shows limited improvement under intermediate fusion, with performance of 61.62 ± 6.43 , lower than its early fusion equivalent. This mirrors the early fusion observations and suggests that CT does not consistently enhance WSI-derived prognosis in this cohort, particularly given the high (64%) WSI missingness.

2.7 Robustness to Modality Dropout and Adaptive Attention

While the intermediate fusion results established the best model performance, we further validated the model’s robustness w.r.t. any modality. Using the best performing

architecture, i.e., the ConcatODST intermediate fusion model, we conducted a controlled missingness analysis by artificially masking single modalities in each test set. Figure 4 reports C-index metric trajectories as the availability of a single targeted modality is progressively reduced from its natural baseline (to complete unavailability (100% missing), while keeping the remaining modalities unchanged.

Beyond evaluating stability, this masking procedure serves as a post-hoc Explainable AI (XAI) mechanism. Specifically, the performance drop induced by suppressing a modality can be interpreted as an estimate of the model’s reliance on that data stream.

Figure 4.a decomposes modality contributions in the trimodal setting and reveals a consistent hierarchy of prognostic relevance. Masking the Tabular modality (red curve) produces a steep and near-monotonic decrease in performance, indicating that clinical variables provide a core prognostic signal that cannot be fully compensated for by imaging alone; this behavior is consistent across all configurations that include Tabular data, i.e., the red curves in *CT+Tabular* and *WSI+Tabular*. Masking WSI (blue curve) also causes a marked performance decrease as availability drops from the already sparse baseline (66.5% missing) to complete absence, suggesting that even a limited number of available slides carries dense prognostic information.

In contrast, removing CT (green curve in Fig. 4.a) does not deteriorate performance; the C-index remains stable and can even increase slightly as CT availability decreases. This pattern is indicative of an adaptive fusion regime in this cohort, where CT representations appear to be not fully aligned with the survival task than Tabular or WSI features in this cohort. Rather than enforcing uniform modality use, ConcatODST appears to learn to attenuate weak or inconsistent inputs, effectively prioritizing the modalities that provide more reliable prognostic evidence. These behaviors can be observed across other bimodal settings (Fig. 4b-d). In *WSI+CT* (Fig. 4.b), masking WSI leads to a sharp degradation, whereas masking CT yields a flatter trajectory, reinforcing that the dominant visual prognostic signal is carried by WSI. In *CT+Tabular* (Fig. 4d), removing Tabular data causes a pronounced collapse in performance, while removing CT has a comparatively smaller effect. Finally, in the best-performing *WSI+Tabular* configuration (Fig. 4c), C-index values degrade when either modality is suppressed, confirming that these two streams provide complementary and high-fidelity information that the model integrates effectively.

Notably, when a bimodal model is forced into a unimodal inference regime (i.e., by masking one modality entirely), performance decreases relative to the full bimodal setting, as expected due to information removal, yet in several cases remains competitive with, or even exceeds, the corresponding unimodal baselines. This behavior can be observed in the *WSI+Tabular* where the removal of the WSI slides yields 67.922, 14 C-index, that is slightly higher than the best performing unimodal ML model trained on Tabular data (RSF, 67.473.61). This suggests that the model does not merely combine independent unimodal predictors, but learns internal representations that remain informative even when only a subset of modalities is available, supporting the practical utility of the proposed missing-aware fusion approach.

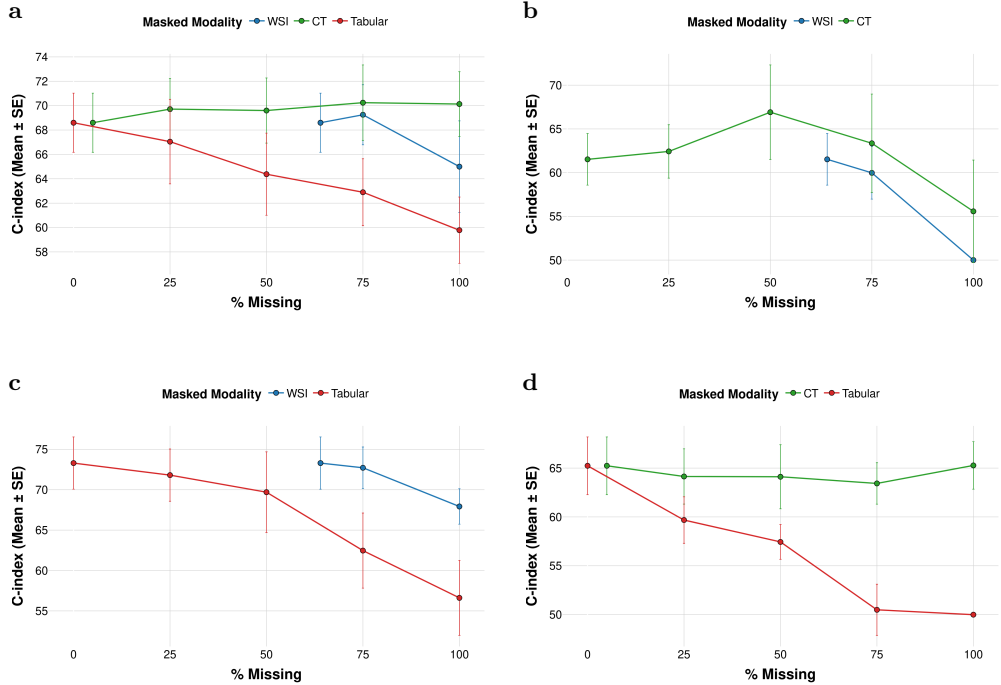


Fig. 4 Performance under increasing missingness for multimodal intermediate fusion combinations. Each panel reports the mean C-index \pm Standard Error over 5 folds. (a) WSI+CT+Tab model. (b) WSI+CT model. (c) WSI+Tabular model. (d) CT+Tabular model.

2.8 Clinical Risk Stratification and Survival Analysis

To assess the translational clinical utility of the intermediate fusion models, we performed an aggregated risk stratification analysis. Risk scores predicted across the 5-fold cross-validation were pooled to form a combined distribution, ensuring a robust evaluation of the entire cohort. An optimal risk threshold was then derived using the log-rank test, partitioning the patient population into *High-Risk* and *Low-Risk* groups. To ensure comparable stratification, this data-driven cutoff was applied across all modality configurations for all the intermediate fusion models.

Survival differences between the defined risk groups were subsequently evaluated using Kaplan–Meier analysis (Figure 5). In the CT+Tabular configuration (Figure 5.a), stratification efficacy was limited; the risk groups exhibited partial overlap, yielding a non-significant log-rank test ($p = 0.1698$). The WSI+CT model (Figure 5.b) demonstrated improved discrimination, approaching statistical significance ($p = 0.0527$). A marked improvement was observed with the WSI+Tabular combination (Figure 5.c), which successfully achieved a statistically significant separation between risk groups ($p = 0.0369$). The strongest stratification emerged from the tri-modal model (Figure 5.d), where the survival curves diverged sharply, resulting in a highly significant distinction ($p = 0.0094$).

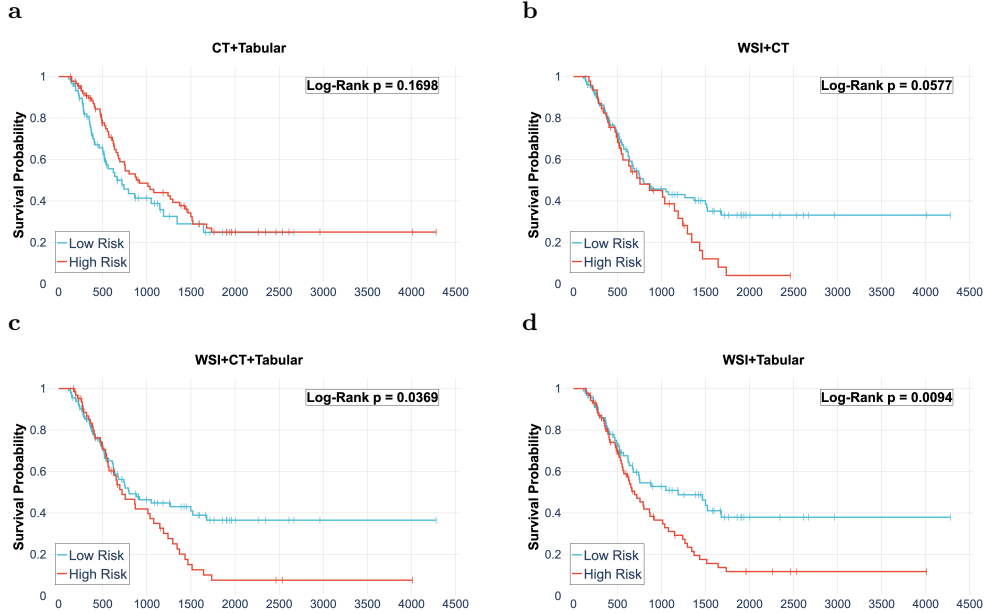


Fig. 5 Stratified Kaplan–Meier survival curves for intermediate fusion models (ConcatODST), with follow-up time (days) on the x-axis and survival probability on the y-axis. Patients are stratified into *Low-Risk* and *High-Risk* groups according to the predicted 5-year outcome score produced by each model. Panels **a–d** report the resulting risk-stratified curves across different modality combinations.

2.9 Clinical Utility: Risk Stratification for Progression Events

Beyond overall survival prediction, the clinical relevance of a prognostic model must be validated in terms of its ability to stratify patients according to clinically meaningful disease events. For this reason, we evaluated whether the proposed risk stratification aligns with the actual progression patterns observed in the cohort, focusing on events that directly reflect disease progression. In this context, two complementary clinical endpoints are of particular relevance: Distant Metastasis (DM), which reflects systemic failure and tumor dissemination beyond the primary site, and Progression-Free Survival (PFS), a composite endpoint capturing local progression, metastatic spread, and survival censoring status.

Figure 6 reports the Kaplan–Meier curves obtained using the scores obtained on all the patients applying the best-performing model, namely the intermediate ConcatODST trained on WSI+Tabular. Patient-specific risk scores were aggregated across test folds and used to stratify individuals into *Low-Risk* and *High-Risk* groups. Survival differences were then evaluated within each risk group, separately for DM (top row) and PFS (bottom row), to assess whether the model’s prognostic signal extends beyond mortality prediction.

For distant metastasis, the model achieves a clear separation between patients who develop metastatic disease and those who remain metastasis-free within both

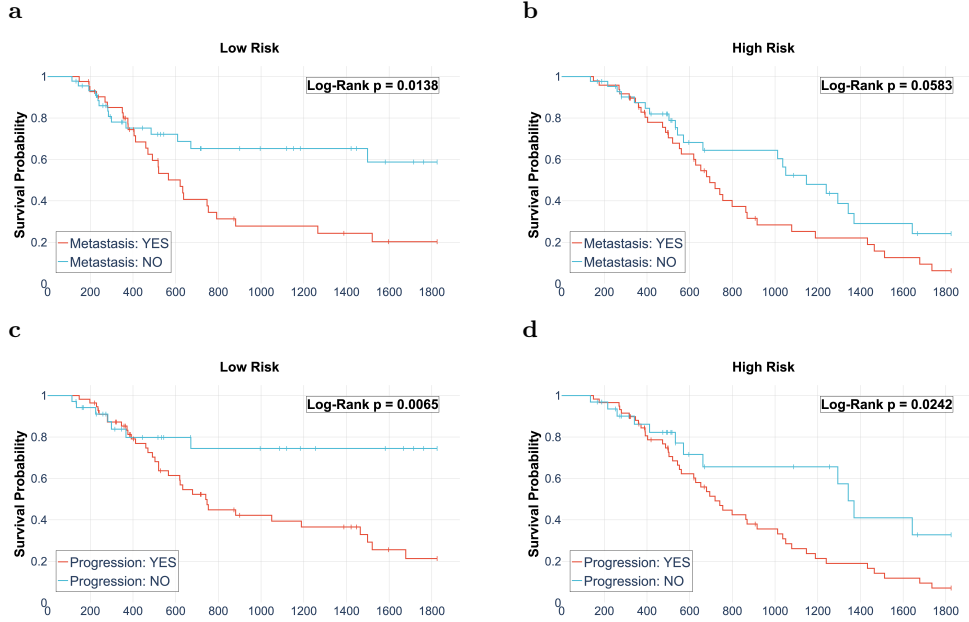


Fig. 6 Kaplan–Meier survival curves for Distant Metastasis (top row) and Progression Free Survival (bottom row) obtained using the WSI–Tabular intermediate configuration. Left: Low-Risk group. Right: High-Risk group.

risk groups. In the Low-Risk group (Fig. 6.a), metastasis-free survival remains high and stable over time, whereas patients who eventually develop metastases exhibit an early and pronounced decline (log-rank $p = 0.0138$). A similar, albeit attenuated, separation is observed in the High-Risk group (Fig. 6.b), where metastatic and non-metastatic trajectories diverge despite the overall worse prognosis (log-rank $p = 0.0583$). These findings indicate that the WSI+Tabular model captures biologically meaningful features associated with metastatic potential.

A comparable pattern emerges for progression-free survival. Within the Low-Risk subgroup (Fig. 6.c), patients without progression display a sustained survival plateau, while those experiencing progression show a continuous decline (log-rank $p = 0.0065$). In the High-Risk subgroup (Fig. 6.d), progression events occur earlier and more frequently; nevertheless, the model continues to distinguish patients with markedly different outcomes (log-rank $p = 0.0242$).

The resulting stratification demonstrates the clinical utility of the proposed approach. By identifying a Low-Risk subpopulation characterized by durable disease control, the model highlights patients who may benefit from less aggressive surveillance strategies. Conversely, the consistent separation observed in the High-Risk group supports its potential role in flagging patients who may require intensified monitoring or treatment escalation.

Despite the promising results, our study acknowledges several limitations that define the scope for future work. First, the analysis is based on a retrospective cohort from a single center ($n = 179$). While the missing-aware framework allowed us to

maximize the effective sample size, external validation on multi-centric datasets is required to confirm the generalizability of the identified prognostic signatures and the robustness of the fusion strategy across different acquisition protocols. Second, the under-performance of the radiological modality compared to pathology and clinical data warrants further investigation. It remains unclear whether this stems from the specific pre-training of the CT FM (Merlin) or intrinsic limitations in the prognostic value of standard staging CTs for this specific task. Future research should explore alternative visual backbones or distinct anatomical regions of interest to better extract radiological patterns. Third, while the intermediate fusion (ConcatODST) proved effective, the fusion mechanism relies on learned concatenation. More complex interactions could be modeled through explicit attention mechanisms (e.g., Cross-Attention) to dynamically weight modalities at the feature level before fusion [Guarrasi et al. \(2025a\)](#). Finally, to translate this methodology into production, future efforts must focus on computational efficiency. The current pipeline involves heavy FM feature extraction; distilling these large models into lightweight encoders would be essential for deployment in clinical environments with limited hardware resources. Expanding this methodology to other oncological settings represents a natural next step, verifying if the synergy between Tabular and WSI data holds across different tumor types and therapeutic contexts.

3 Discussion

This study investigates missing-aware multimodal survival modeling in locally advanced NSCLC by integrating CT, WSI, and structured clinical variables within a unified time-to-event learning framework. While multimodal deep learning (MDL) is often presented as a natural route to precision prognosis, its clinical translation is systematically hindered by a practical paradox: as the number of required diagnostic streams increases, the probability of observing a complete patient profile sharply decreases. In our cohort, a complete-case design would have excluded 77.1% of patients (Section 2.2), introducing substantial selection bias and undermining the clinical representativeness of downstream models. By adopting a missing-aware intermediate-fusion pipeline (ConcatODST), we show that survival prediction can be learned on the full cohort without modality imputation, treating missingness as a structural property of oncology data rather than an exception.

Our representation-space analysis (Section 2.5) revealed a clear modality-dependent pattern in the prognostic information captured by the extracted embeddings. CT representations obtained with Merlin exhibited a certain degree group separability with respect to mortality status, suggesting that the radiological encoder captures a macroscopic signal that is aligned, at least partially, with outcome survival outcomes for this cohort. By contrast, WSI embeddings did not show clear linear separation in the raw feature space, yet they became strongly predictive once processed by unimodal or the multimodal models (Section 2.6).

Similarly, the tabular representation space displayed substantial overlap between outcome groups, consistent with the fact that structured clinical variables are heterogeneous and rarely separable in an unsupervised embedding space. To further

contextualize the clinical stream, we also reported a univariate analysis of baseline variables after stratifying patients into *Survivors* and *Non-Survivors*. Although this exploratory analysis is not intended to replace the time-to-event formulation, it provides an interpretable characterization of how individual covariates relate to outcome status, mirroring standard clinical reporting and helping to disentangle the marginal associations that underlie overall survival differences in the cohort.

Overall, these findings emphasize that the utility of pretrained representations is modality- and task-dependent: separability in the embedding space is neither necessary nor sufficient for strong survival performance, and the alignment between pretraining objectives and prognostic endpoints remains a key determinant of downstream efficacy.

A key contribution of this work is an empirical analysis of *intermediate fusion* under missingness, rather than the introduction of a novel fusion strategy. ConcatODST provides a controlled and structured intermediate-fusion that is well suited to quantify multimodal complementarity in small and sparse cohorts. Within this setting, the strongest performance consistently emerged from the **WSI+Tabular** configuration (peaking at C -index ≈ 0.73), outperforming the trimodal configuration (Section 2.6). This pattern suggests that, for this cohort, the most salient prognostic information is captured by the interaction between microscopic tissue architecture and tumor biology (WSI) and the systemic patient status and treatment context (Tabular). The reduced performance obtained in the trimodal configuration indicates that CT features may introduce variance that is not consistently informative for survival in this setting. Rather than contradicting the clinical relevance of imaging, this result underscores a practical modeling point: when features are extracted via general-purpose FMs and the training cohort is limited, additional modalities can dilute signal if their representations are not well aligned with the endpoint or if they are redundantly captured by other streams.

The controlled masking experiments (Section 2.7) further clarify how the model behaves under incomplete profiles. Performance degraded sharply when Tabular inputs were removed, and decreased substantially when WSI availability was reduced from an already missing baseline ($\sim 66\%$ missing WSI), confirming that these two streams carry the core prognostic signal. Conversely, masking CT did not reduce performance, consistent with the best resulting intermediate fusion model (**WSI+Tabular**), this behavior confirms that the fusion head ignores modalities not informative for the survival tasks rather than exploiting every available input. From a deployment standpoint, this behavior is desirable: it suggests the model can remain stable when a modality is missing or when a modality is present but not reliably informative for the specific patient distribution.

Beyond aggregate performance, the framework demonstrated clinically meaningful stratification behavior (Section 2.8). Risk groups derived from the intermediate-fusion models separated survival trajectories, and the specific analysis on the best-performing WSI+Tabular intermediate fusion configuration further shows the capacity of the model to stratify systemic progression patterns, including distant metastasis and progression-free survival. These results support the interpretation that the learned risk score is not merely a statistical artifact of mortality labeling, but reflects clinically relevant failure modes that drive outcome heterogeneity in unresectable stage

II–III NSCLC. In practice, such stratification could support risk-adapted follow-up and treatment intensification decisions, motivating prospective validation as a clinical decision-support signal.

Despite the promising results, our study acknowledges several limitations that define the scope for future work. First, it is based on a single-center cohort with limited sample size ($n = 179$ after eligibility filtering), and external validation across institutions and acquisition protocols is essential to confirm generalizability. Second, the relatively modest contribution of CT features warrants deeper investigation: future work should test alternative CT extraction backbones, endpoint-aligned fine-tuning strategies, and more explicit anatomical conditioning (e.g., multi-region or tumor-aware representations) to avoid relying on broad systemic processes. Third, while intermediate fusion proved effective, we intentionally restricted the study to a structured and reproducible intermediate-fusion baseline (ConcatODST) to isolate the effect of missing-aware multimodal learning. Exploring more expressive intermediate fusion mechanisms, e.g., cross-attention or gating modules that dynamically weight modalities and learn higher-order interactions, is a natural next step, but is left to future work to avoid conflating architectural novelty with cohort-specific conclusions. Finally, computational cost remains a barrier: FM-based pre-processing is heavy, and practical translation will likely require distillation or lightweight surrogates for feature extraction, alongside streamlined inference pathways.

In summary, our results indicate that missing-aware intermediate fusion can deliver robust survival prediction under realistic clinical sparsity, with the strongest and most stable gains arising from the synergy between histopathology and structured clinical context. This supports a pragmatic roadmap for MDL in oncology: prioritize architectures that are missing-native, benchmark modality complementarity under natural missingness, and only then pursue more complex fusion operators once the data regime and signal alignment are empirically established.

4 Materials

Dataset and Cohort Selection

Data collection was carried out at the *Fondazione Policlinico Universitario Campus Bio-Medico of Rome* and encompassed 353 patients with histologically confirmed Non-Small Cell Lung Cancer (NSCLC), all diagnosed at stage II–III following the 9th edition TNM classification of lung cancer [Detterbeck et al. \(2024\)](#) and enrolled retrospectively or prospectively between 2012 and 2024.

From this cohort, we retained only individuals classified as unresectable stage II–III disease [Daly et al. \(2021\)](#) (IIA, IIB, IIIA, IIIB, or IIIC) using the 9th edition of the TNM classification for Thoracic Oncology [Detterbeck et al. \(2024\)](#). Accordingly, the study employed the following exclusion criteria to ensure a homogeneous cohort: (i) patients with resectable tumors who underwent surgery in neoadjuvant settings; (ii) patients treated with palliative intent; (iii) cases with incomplete baseline clinical information or missing follow-up; (iv) small cell lung cancers patients. In addition, we removed patients with non-NSCLC histologies, metastatic or recurrent disease at presentation, prior thoracic surgery or postoperative RT/RTCT, those managed with

non-standard therapeutic pathways (e.g., SBRT alone or systemic therapy only), and cases lacking verifiable diagnostic imaging or pathology.

After applying these criteria, the final study population consisted of 179 patients, providing a homogeneous cohort representative of the clinical course of locally advanced, non-resectable NSCLC. For every included patient, a comprehensive set of structured clinical variables was curated to capture the biological profile and treatment history. As detailed in Tables 1 and 2, data collection was stratified into four key domains: (i) *general characteristics*, including demographic and physiological baselines such as sex, age, weight, height, smoking status, daily cigarette consumption, family history of neoplasms, numeric pain rating scale (NRS), and specific comorbidity profiles (vascular, metabolic, renal, pulmonary); (ii) *tumor biology*, encompassing histological subtype (adenocarcinoma, squamous cell carcinoma, NOS), TNM classification, molecular biomarkers (EGFR, ALK, MET, PD-L1), and other biopsy details; (iii) *treatment parameters*, covering chemotherapy details (induction cycles, specific drug schemes), radiotherapy metrics (total dose, fractionation, technique, duration), treatment interruptions, and the administration of adjuvant immunotherapy; and (iv) *toxicity and outcomes*, recording grade-specific adverse events (esophageal, pulmonary, hematological).

Beyond Overall Survival (OS), the study incorporated a comprehensive assessment of disease progression patterns to characterize failure modes. Secondary clinical endpoints included: (i) *distant Metastasis (M)*, indicating systemic disease spread to non-contiguous organs; and (ii) *Progression-Free Survival (PFS)*, calculated as the time from treatment initiation to the first documented event of local and distant progression or death.

Imaging Acquisition

For each patient, multimodal imaging data were systematically acquired prior to the initiation of radical therapy to establish a baseline for prognostic modeling.

- **Radiology.** CT scans were retrospectively retrieved from the institutional Picture Archiving and Communication System (PACS). Specifically, we collected the *treatment planning CTs* acquired within 30 days prior to the start of Chemoradiotherapy. Unlike standard diagnostic scans, these planning CTs are acquired under rigorous protocols to ensure geometric accuracy for dose calculation, providing a standardized and reproducible representation of the macroscopic tumor burden and thoracic anatomy across the entire cohort.
- **Pathology.** High-resolution Whole Slide Images (WSIs) were generated from diagnostic tissue biopsies obtained via bronchoscopy or CT-guided percutaneous needle aspiration. Formalin-fixed paraffin-embedded (FFPE) tissue blocks were sectioned and stained with Hematoxylin and Eosin (H&E) according to standard clinical workflows. Subsequently, the physical glass slides were digitized at 20 \times magnification (0.5 μ m/pixel) using a high-throughput slide scanner. This digitization process transformed the analog histological samples into gigapixel-resolution digital slides, ensuring the preservation of the intricate microscopic tumor architecture and cellular phenotypes required for computational analysis.

Ethical approval

Data collection spans two regulatory phases: a retrospective phase approved on October 30, 2012, and registered on *ClinicalTrials.gov* (Identifier: NCT03583723), and the prospective phase was approved on 16 April 2019 with identifier 16/19 OSS. All patients provided written informed consent for the use of their clinical and imaging data for research purposes.

5 Methods

5.1 Framework Overview

We propose a three-stage multimodal framework designed to predict survival outcomes from incomplete heterogeneous data. As illustrated in Figure 2, the pipeline consists of: (1) Unimodal feature extraction using pre-trained FM to bypass data scarcity; (2) Missing-aware representation learning using the NAIM architecture; and (3) our proposed intermediate fusion strategy.

5.1.1 Step 1: Preprocessing & Feature Extraction

We formalize the three-stage multimodal learning pipeline illustrated in Fig. 2. Given three heterogeneous input modalities, Tabular (x_1); CT (x_2), and WSI (x_3), the goal is to construct a unified representation for downstream survival prediction. We denote by $\Phi_i : \mathcal{X}_i \rightarrow \mathbb{R}^{d_i}$ the modality-specific feature extractors producing high-level embeddings $x_i^* \in \mathbb{R}^{d_i}$ leveraging state of the art FMs for each modalities or classical pre-processing pipelines.

Tabular Data (x_1).

To ensure consistency during model training, all clinical features underwent a standardized preprocessing pipeline. Categorical variables (e.g., comorbidities, histology) were one-hot encoded, while ordinal features (e.g., disease stage, ECOG status) were integer-encoded to preserve their inherent hierarchy. Numerical features (e.g., age, weight) were standardized via z-score normalization to zero mean and unit variance. The resulting feature vector is denoted as $x_1^* = \Phi_1(x_1)$, where Φ_1 represents the composite preprocessing function.

Radiology Imaging (x_2).

Volumetric radiological features are extracted using Merlin [Blankemeier et al. \(2024\)](#), a 3D Vision Transformer (ViT) based FM. Merlin is pre-trained via a CLIP-style objective on massive multimodal datasets of paired CT volumes and radiology reports, enabling it to learn semantically rich anatomical representations. To ensure consistency with the Merlin encoding pipeline, raw CT volumes undergo the following standardized preprocessing steps: (i) *Resampling*: all volumes are resampled to a uniform isotropic resolution of $1.5 \times 1.5 \times 3.0 \text{ mm}^3$ via bilinear interpolation to correct for eventual spacing variability. (ii) *Windowing & Normalization*: Voxel intensities are clipped using a standard lung window (center = 0 HU, width = 2000 HU), ensuring that out-of-range values are suppressed. The windowed volumes are then normalized to the $[0, 1]$ interval

via min-max scaling. (iii) *Cropping*: the extraction is performed on the whole body volume. We center crop the resampled volume to a final size of $224 \times 224 \times 160$ voxels, to ensure uniform input dimensions for the Merlin encoder. The processed volume x_2 is passed to the Merlin encoder, \mathcal{E}_{CT} , to yield the final features representation in a single output vector with 2048 dimensions. Here follow the notation:

$$x_2^* = \Phi_2(x_2) = \mathcal{E}_{CT}(x_2) \in \mathbb{R}^{2048} \quad (1)$$

***Pathology Imaging* (x_3)**

To capture the microscopic tumor characterization, we utilize a hierarchical encoding pipeline to extract a unique representation vector for each WSI. First, WSIs are processed using CLAM [Lu et al. \(2021\)](#) (CLustering-constrained Attention Multiple instance learning) with the objective to segment tissue from background artifacts. From each WSI (x_3), we extract a slide-specific set of tissue-containing image tiles. After tissue segmentation, all background and artefactual regions are removed, and the remaining tissue area is decomposed into a non-uniform number N_w of non-overlapping patches of size 256×256 pixels at $20\times$ magnification. For each x_3 , we denote this patch set as $P_w(x_3) = \{p_j\}_{j=1}^{N_w}$, where each element p_j corresponds to a spatially localized region that retains diagnostically meaningful microscopic information. This patch-based decomposition allows the model to focus on localized morphological patterns that would otherwise be diluted at whole-slide scale.

Each patch $p_j \in P_w$ is then projected into a descriptive 512-dimensions embedding using the vision encoder of MI-Zero [Lu et al. \(2023\)](#) (\mathcal{E}_{patch}), a vision-language foundation model pre-trained to align visual features with semantic pathology descriptions. Eq. 2 formalizes the projection step:

$$\mathbf{z}_j = \mathcal{E}_{patch}(p_j) \in \mathbb{R}^{512}, \quad p_j \in P_w \quad (2)$$

Finally, TITAN [Ding et al. \(2025\)](#)(Transformer-based pathology Image and Text Alignment Network), \mathcal{E}_{wsi} , aggregates the sequence of patch embeddings into a unified latent representation with 768 dimensions. TITAN leverages a self-supervised masked prediction task to coherently synthesize local cellular phenotypes into a global descriptor. We indicate the final slide-level feature vector in the following Eq.3:

$$x_3^* = \mathcal{E}_{wsi}(\{\mathbf{z}_j\}_{j=1}^{N_w}) \in \mathbb{R}^{768}. \quad (3)$$

By structuring the WSI into interpretable units and encoding them consistently, this pipeline preserves fine-grained microscopic details while ensuring that the representation is compatible with the subsequent multimodal fusion stages. The complete preprocessing pipeline Φ_3 , representing the composition of patching, encoding, and aggregation, is formalized as:

$$x_3^* = \Phi_3(x_3) = \mathcal{E}_{wsi}(\mathcal{E}_{patch}(p_j)) \in \mathbb{R}^{768}; p_j \in P_w(x_3). \quad (4)$$

5.1.2 Step 2: Missing-Aware Unimodal Encoding (NAIM)

To robustly accommodate structural missingness, we employ the Not Another Imputation Method (NAIM) [Caruso et al. \(2024b\)](#) model. Standard deep learning models require complete input vectors; traditionally, this forces researchers to use *imputation* (replacing missing values with means, medians, or synthetic guesses), which inevitably introduces noise and bias. NAIM offers a fundamental paradigm shift: rather than synthesizing fake data, the network is architected to *dynamically ignore* absent information. In our framework, we instantiate a separate NAIM encoder F_i for each modality. Each encoder takes as input the raw feature vector x_i^* (from Step 1) and a binary mask $M_i \in \{0, 1\}^K$ (where 1 indicates missing), projecting them into a robust latent representation h_i .

Dual-Stream Feature Embedding.

The first challenge is to convert heterogeneous data (continuous numbers, categorical classes, and missing values) into a unified high-dimensional space where they can interact. NAIM achieves this via a dual embedding strategy that treats "missingness" not as a null value, but as a specific structural state.

- **Categorical Features (x^{cat}):** Discrete variables (e.g., histology, sex) are mapped using a learnable lookup table E^{cat} . If a feature value is present, the lookup table selects the corresponding trainable embedding vector; if the value is missing, the encoder instead retrieves the frozen padding vector. Formally, for the j -th categorical feature, the embedding is defined in Eq. 5.

$$e_j^{cat} = b_j + E_j^{cat}(x_j^{cat}), \quad (5)$$

where b_j is a learnable bias term specific to that feature index.

- **Numerical Features (x^{num}):** Continuous variables (e.g., age, tumor volume) require a more nuanced approach to preserve their magnitude. We employ a specialized lookup table E^{num} containing only two vectors: $\mathbf{v}_{present}$ (trainable) and $\mathbf{v}_{missing}$ (frozen zeros). If the feature is missing, the embedding is simply the bias term plus the zero vector. If the feature is present, we multiply the trainable $\mathbf{v}_{present}$ vector by the scalar value of the feature x_j^{num} . We formulate the numerical embedding in the following equation:

$$e_j^{num} = b_j + x_j^{num} \cdot E_j^{num}(\mathbb{I}_{present}), \quad (6)$$

where $\mathbb{I}_{present}$ is the indicator index. This mechanism allows the network to learn the *significance* of the feature via $\mathbf{v}_{present}$ while scaling it by the actual patient data.

Double-Sided Masked Attention.

Once the data is tokenized into embeddings, it is processed by the NAIM Transformer encoder. However, standard self-attention mechanisms would fail because missing tokens would still participate in the softmax normalization, corrupting the attention distribution. NAIM solves this via a double-sided masking strategy. The goal is to

ensure that a missing feature neither *casts* attention (influencing others) nor *receives* attention (being updated by others).

Let Q, K, V be the query, key, and value matrices derived from the input embeddings. We define a mask matrix \mathbf{M} , where $\mathbf{M}_{ij} = -\infty$ if either feature i or feature j is missing, and 0 otherwise. The resulting formulation, reported in Eq. 7, applies the mask before and after the softmax operation, thereby enforcing a complete suppression of missing-feature interactions:

$$\mathbf{A}(Q, K, V) = \text{ReLU} \left(\mathcal{S} \left(\frac{QK^\top}{\sqrt{d_h}} + \mathbf{M} \right) + \mathbf{M}^\top \right) V. \quad (7)$$

Where \mathcal{S} is the softmax operator. This bidirectional exclusion guarantees that the attention mechanism operates solely on observed features, preserving the functionality of the learned representations even under substantial missingness. Here is how this mechanism works step-by-step:

1. $\frac{QK^\top}{\sqrt{d_h}} + \mathbf{M}$: Adding $-\infty$ to the attention scores forces the corresponding softmax, values to exactly zero.
2. $+\mathbf{M}^\top$: we add the mask again (transposed) after the softmax. This is a crucial reinforcement step that explicitly zeros out any residual connection *from* a missing feature to others.
3. ReLU: Ensures non-negativity and sparsity in the final attention map.

This mechanism ensures that gradients propagate *only* through observed data paths, effectively creating an architecture that changes structure based on which data are available for a specific patient.

NAIM Encoders for Unimodal Survival Prediction

Each modality is processed independently using a dedicated NAIM encoder. Unlike standard architectures that treat the input as a monolithic vector, NAIM tokenizes the input modality x_i into a sequence of distinct feature embeddings (as defined in Eqs. 5–6). These tokens are processed via the masked self-attention mechanism, which captures intra-modality correlations while strictly preventing information leakage from missing values. The resulting sequence of contextualized embeddings is then flattened to form the comprehensive unimodal representation $h_i \in \mathbb{R}^{d_{model}}$.

To translate the robust latent representation h_i into a continuous survival prediction, the embedding is passed through a hybrid head composed of an *Oblivious Differentiable Survival Tree* (ODST) [Langley and Sage \(1994\)](#), noted as E_i , followed by a Fully Connected (FC) layer. The ODST architecture bridges the gap between the interpretability of decision trees and the gradient-based optimization of DL. Unlike standard decision trees, which rely on greedy, hierarchical splits, an *oblivious* tree applies a uniform splitting criterion across all nodes at a given depth. In our differentiable implementation, this hard splitting logic is relaxed using a soft gating function (e.g., sigmoid), enabling the entire ensemble to be optimized end-to-end via backpropagation. Formally, the ODST block maps the unimodal embedding h_i to a structured intermediate representation, capturing non-linear interactions between features. This transformed vector is then projected by a the FC layer to produce the scalar risk score

y_i , as defined in Eq. 8:

$$y_i = \text{FC}\left(\mathbf{E}_i(h_i)\right). \quad (8)$$

Optimization Objective.

Based on the Cox proportional hazards model, The entire pipeline is trained end-to-end by minimizing the negative log partial likelihood loss [Tong et al. \(2020\)](#). Let N_{ob} be the total number of observed events in a batch. The loss function \mathcal{L}_{sur} is defined as:

$$\mathcal{L}_{sur} = -\frac{1}{N_{ob}} \sum_{i:C_i=1} \left(y_i - \log \sum_{j:T_j \geq T_i} e^{y_j} \right), \quad (9)$$

where:

- $C_i = 1$ indicates the occurrence of the event for patient i (uncensored).
- y_i is the hazard risk score predicted by the network for patient i .
- T_i and T_j denote the observed survival times for patient i and j , respectively.
- The inner summation $\sum_{j:T_j \geq T_i}$ aggregates the risk over the set of all patients j still at risk at time T_i .

This objective enforces the correct relative ordering of survival times by penalizing the model when a patient who experienced an event earlier is assigned a lower risk score than those who survived longer.

5.1.3 Step 3: Intermediate Fusion and Multimodal Survival Prediction

The framework subsequently transitions to the proposed **intermediate fusion** strategy. Each modality is processed by its dedicated NAIM encoder and each ODST layer (as detailed in Sec. 5.1.2), producing three uniform robust latent representations: h_1 (Tabular), h_2 (CT), and h_3 (WSI). These embeddings capture modality-specific abstractions while being explicitly conditioned to handle missingness via the double-sided masking mechanism (Eq. 7).

To construct the unified multimodal patient profile, the individual latent vectors are fused together via concatenation (\oplus):

$$h_m = \oplus(h_1, h_2, h_3) \in \mathbb{R}^{d_1+d_2+d_3}. \quad (10)$$

This fused vector h_m retains complementary prognostic signals from each data source. In the proposed multimodal configuration, referred to as **ConcatODST**, the fused representation is passed to the final ODST module E_m followed by a fully connected regression layer, mirroring the structure used in the unimodal head described in Eq. 8. In this stage, E_m learns non-linear interactions across the unimodal embeddings to produce the final risk score y_m .

The multimodal pipeline is fine-tuned end-to-end using the \mathcal{L}_{sur} objective defined in Eq. 9.

5.2 Model Comparison and Training Strategy

To evaluate the proposed intermediate fusion framework, we conducted a structured benchmarking analysis comparing different architectural paradigms, integration strategies, and established ML baselines.

Unimodal Baselines and Ablation Study

Before assessing multimodal fusion, we examined the performance of each modality independently through a unimodal ablation study. For Tabular, CT, and WSI data, we compared the following configurations:

- Machine learning baselines: Cox Proportional Hazards (CPH), Random Survival Forests (RSF), and Survival Gradient Boosting (SGB), trained on the extracted features.
- Standard Neural Network (NN): a baseline model using the feature embedding layer, as described in Section 5.1.2, followed by a multi-layer perceptron with ReLU activations.
- NAIM (encoder-only): the NAIM encoder paired with a linear survival head, isolating the contribution of the masked attention mechanism.
- NAIM + ODST: the complete unimodal model combining the NAIM encoder with the ODST survival head.

Multimodal Fusion Strategies.

To isolate the contribution of the intermediate fusion architecture, we benchmarked it against two alternative integration paradigms, adopting a consistent integration framework (concatenation + ODST head) but varying the optimization scope:

- **Early Fusion (ConcatODST^{*}):** Integration is performed directly at the embedding level. Robust latent representations are extracted from the *pre-trained* unimodal NAIM+ODST encoders (frozen) and concatenated into a single unified vector, $x_{\text{early}} = \oplus(h_1, h_2, h_3)$. This combined vector is fed directly into the ODST+FC survival head, structurally identical to the one used in the intermediate architecture. By keeping the upstream encoders frozen, this baseline explicitly tests the additive predictive power of the learned unimodal features in isolation, without the synergistic benefits of joint end-to-end optimization.
- **Intermediate Fusion (ConcatODST):** In this proposed approach, the architecture is identical to early fusion, but optimization is performed *end-to-end*. The unimodal encoders remain trainable, allowing the backpropagation of gradients from the multimodal ODST head through to the modality-specific branches. This enables the encoders to adapt their feature representations to maximize cross-modal synergy.
- **Late Fusion (Ensemble Ranking):** Integration at the prediction level. Independent unimodal models (NAIM+ODST) are trained separately for each available modality. At inference time, we employ a *ranking-based ensemble*: risk scores from each unimodal model are converted into ranks (ordering the cohort from lowest to

highest risk). The final multimodal risk score is the sum of these ranks:

$$\text{Rank}_{\text{final}} = \sum_{m \in \mathcal{M}} \text{Rank}(y_m),$$

where \mathcal{M} is the set of available modalities. This non-parametric aggregation assumes no synergistic interaction between modalities.

Experimental Setup

To mitigate overfitting and ensure robust performance estimation, we employed a stratified 5-fold cross-validation strategy. The dataset was partitioned into 5 non-overlapping folds, preserving the ratio of events to censored patients. In each iteration, 3 folds were used for training, 1 for validation and 1 for testing. This procedure was repeated 5 times, and final metrics are reported as the mean \pm standard deviation. Optimization utilized the *AdamW* optimizer (weight decay 1×10^{-5}) with a batch size of 32 for all the training approaches. Training ran for a maximum of 500 epochs with early stopping (patience equal to 50 epochs) based on the loss computed on the validation set. validation.

To ensure a fair comparison across fusion paradigms, we adopted a unified two-stage training protocol. In the early fusion setting (ConcatODST*), the NAIM encoders were initialized using weights obtained during unimodal pre-training and kept frozen throughout training. In the intermediate fusion setting (ConcatODST), the encoders were initialized identically but remained trainable, enabling end-to-end optimization in which gradients from the survival loss refine modality-specific representations.

The learning rate schedule (η) was defined within the range $\eta_{\min} = 10^{-8}$ to $\eta_{\max} = 10^{-5}$ and consisted of three components. First, a linear warm-up over the initial 50 epochs increased η from η_{\min} to η_{\max} to avoid early training instability. After warm-up, a plateau detector monitored the validation loss; if no improvement was observed for 20 epochs, a decay schedule was initiated to anneal η back to η_{\min} across 12 steps. Training was halted if the validation metric failed to improve for 50 consecutive epochs.

During end-to-end optimization of the intermediate fusion model, we adopted differential learning rates to balance stability and plasticity. The multimodal ODST and fully connected layers were updated using the full learning-rate range (up to $\eta_{\max} = 10^{-5}$), while the pretrained unimodal encoders used a tenfold smaller rate (effective $\eta_{\max} = 10^{-6}$), preserving established feature representations while allowing controlled adaptation during cross-modal alignment. All models were implemented in PyTorch and trained on a single *NVIDIA A40 GPU* (48GB VRAM).

Evaluation Metrics

Model discrimination was quantified using the *Concordance Index (C-index)*, which measures the probability that, for a random pair of subjects, the subject who experienced the event earlier has a higher predicted risk score. To rigorously account for potential censoring bias, we reported also the *Uno's C-index* [young Park et al. \(2021\)](#). The latter relies on *Inverse Probability of Censoring Weights* (IPCW) to correct for

the unequal probability that individuals remain uncensored over time. By weighting each observation by the inverse of its estimated probability of being uncensored, IPCW compensates for informative censoring and yields a consistent measure of discriminative performance even when the censoring mechanism depends on patient covariates. Lastly, to assess predictive performance over the follow-up period, we computed the *time-dependent Area Under the Curve* (td-AUC). Specifically, we evaluated the mean cumulative dynamic AUC at the 25th, 50th, and 75th percentiles of the observed event times in the test set.

Statistical Analysis

Continuous variables are reported as mean \pm standard deviation, categorical variables as frequencies (n , %). Baseline comparisons utilized the Chi-square test (categorical) and one-way ANOVA (continuous). Survival curves were estimated via the Kaplan-Meier method and compared using the Log-Rank test. Statistical significance was set at a two-sided $p < 0.05$. All analyses were conducted in Python (sciPy, lifelines and scikit-learn).

Acknowledgments

Filippo Ruffini is a PhD student enrolled in the National PhD in Artificial Intelligence, XXXVIII cycle, course on Health and life sciences, organized by Università Campus Bio-Medico di Roma. This work was partially supported by: i) PRIN 2022 MUR 20228MZFAA- AIDA (CUP C53D23003620008, CUP H53D23003480006), ii) PNRR MUR project PE0000013-FAIR, iii) PNRR – DM 118/2023, iv) Kempe Foundation under grant no. JCSMK24-0094, v) *Strategic University Projects* “IDEA: AI-powered Digital Twin for next-generation lung cancEr cAre” financed by *Università Campus Bio- Medico di Roma* 2023 (GEN0469). Resources are provided by the *National Academic Infrastructure for Supercomputing in Sweden* (NAIIS) and the *Swedish National Infrastructure for Computing* (SNIC) at Alvis @ C3SE, partially funded by the Swedish Research Council through grant agreements no. 2022-06725 and no. 2018-05973.

References

Blankemeier L, Cohen JP, Kumar A, et al (2024) Merlin: A vision language foundation model for 3d computed tomography. Research Square pp rs-3

Bommasani R (2021) On the opportunities and risks of foundation models. arXiv preprint arXiv:210807258

Captier N, Lerousseau M, Orlhac F, et al (2025) Integration of clinical, pathological, radiological, and transcriptomic data improves prediction for first-line immunotherapy outcome in metastatic non-small cell lung cancer. Nature Communications 16. <https://doi.org/10.1038/s41467-025-55847-5>

Caruso CM, Guerrasi V, Ramella S, et al (2024a) A deep learning approach for overall survival prediction in lung cancer with missing values. Computer Methods and Programs in Biomedicine 254:108308

Caruso CM, Soda P, Guerrasi V (2024b) Not another imputation method: A transformer-based model for missing values in tabular datasets. arXiv preprint arXiv:240711540

Daly M, Singh N, Ismaila N, et al (2021) Management of stage iii non-small-cell lung cancer: Asco guideline. Journal of Clinical Oncology 40:1356 – 1384. <https://doi.org/10.1200/jco.21.02528>

Detterbeck FC, Woodard GA, Bader AS, et al (2024) The proposed ninth edition tn m classification of lung cancer. Chest 166(4):882–895

Ding T, Wagner SJ, Song AH, et al (2025) A multimodal whole-slide foundation model for pathology. Nature Medicine pp 1–13

Graf R, Todd S, Baksh M (2025) Comparison of the cox proportional hazards model and random survival forest algorithm for predicting patient-specific survival probabilities in clinical trial data. ArXiv abs/2502.03119. <https://doi.org/10.48550/arxiv.2502.03119>

Guerrasi V, Tronchin L, Albano D, et al (2024) Multimodal explainability via latent shift applied to covid-19 stratification. Pattern Recognition 156:110825

Guerrasi V, Aksu F, Caruso CM, et al (2025a) A systematic review of intermediate fusion in multimodal deep learning for biomedical applications. Image and Vision Computing p 105509

Guerrasi V, Bertgren A, Näslund U, et al (2025b) Beyond unimodal analysis: Multimodal ensemble learning for enhanced assessment of atherosclerotic disease progression. Computerized Medical Imaging and Graphics p 102617

Guedes J, Woldmar N, Szasz AM, et al (2025) A perspective on integrating digital pathology, proteomics, clinical data and ai analytics in cancer research. Journal of proteomics p 105493

Hanika T, Hirth J (2023) Conceptual views on tree ensemble classifiers. International Journal of Approximate Reasoning 159:108930

Huang Q, Li Y, Huang Y, et al (2025) Advances in molecular pathology and therapy of non-small cell lung cancer. Signal Transduction and Targeted Therapy 10(1):186

Langley P, Sage S (1994) Oblivious decision trees and abstract cases. In: Working notes of the AAAI-94 workshop on case-based reasoning, Seattle, WA, pp 113–117

Lee C, Brown C, Gralla R, et al (2013) Impact of egfr inhibitor in non-small cell lung cancer on progression-free and overall survival: a meta-analysis. *Journal of the National Cancer Institute* 105 9:595–605. <https://doi.org/10.1093/jnci/djt072>

Lee J, Jang J, Eum H, et al (2025) Gliosurv: interpretable transformer for multimodal, individualized survival prediction in diffuse glioma. *npj Digital Medicine* 8(1):660

Li X, Zhao L, Zhang L, et al (2024) Artificial general intelligence for medical imaging analysis. *IEEE Reviews in Biomedical Engineering*

Lobato-Delgado B, Priego-Torres B, Sanchez-Morillo D (2022) Combining molecular, imaging, and clinical data analysis for predicting cancer prognosis. *Cancers* 14(13):3215

Lu MY, Williamson DF, Chen TY, et al (2021) Data-efficient and weakly supervised computational pathology on whole-slide images. *Nature Biomedical Engineering* 5(6):555–570

Lu MY, Chen B, Zhang A, et al (2023) Visual language pretrained multiple instance zero-shot transfer for histopathology images. *Proceedings of the IEEE/CVF Conference on Computer Vision and Pattern Recognition (CVPR)* pp 19764–19775

Machin D, Cheung YB, Parmar M (2006) *Survival analysis: a practical approach*. John Wiley & Sons

Niu Y, bing Xie H, Jia HB, et al (2025) Multimodal deep learning integrating tumor radiomics and mediastinal adiposity improves survival prediction in non-small cell lung cancer: A prognostic modeling study. *Cancer Medicine* 14. <https://doi.org/10.1002/cam4.71077>

Oh S, Kang SR, Oh IJ, et al (2023) Deep learning model integrating positron emission tomography and clinical data for prognosis prediction in non-small cell lung cancer patients. *BMC bioinformatics* 24(1):39

young Park S, Park JE, Kim H, et al (2021) Review of statistical methods for evaluating the performance of survival or other time-to-event prediction models (from conventional to deep learning approaches). *Korean Journal of Radiology* 22:1697 – 1707. <https://doi.org/10.3348/kjr.2021.0223>

Paverd H, Zormpas-Petridis K, Clayton H, et al (2024) Radiology and multi-scale data integration for precision oncology. *NPJ Precision Oncology* 8(1):158

Peng J, Pond GR, Donovan EK, et al (2019) A comparison of radiation techniques in patients treated with concurrent chemoradiation for stage iii non-small cell lung cancer. *International journal of radiation oncology, biology, physics* URL <https://api.semanticscholar.org/CorpusID:211015379>

Ruffini F, Aylon EM, Shen L, et al (2025) Benchmarking foundation models and parameter-efficient fine-tuning for prognosis prediction in medical imaging. arXiv preprint arXiv:250618434

Soenksen L, Ma Y, Zeng C, et al (2022) Integrated multimodal artificial intelligence framework for healthcare applications. *NPJ Digital Medicine* 5. <https://doi.org/10.1038/s41746-022-00689-4>

Spigel D, Faivre-Finn C, Gray J, et al (2022) Five-year survival outcomes from the pacific trial: Durvalumab after chemoradiotherapy in stage iii non-small-cell lung cancer. *Journal of Clinical Oncology* 40:1301 – 1311. <https://doi.org/10.1200/jco.21.01308>

Teoh JR, Dong J, Zuo X, et al (2024) Advancing healthcare through multimodal data fusion: a comprehensive review of techniques and applications. *PeerJ Computer Science* 10:e2298

Tong L, Mitchel J, Chatlin K, et al (2020) Deep learning based feature-level integration of multi-omics data for breast cancer patients survival analysis. *BMC medical informatics and decision making* 20(1):225

Vincent T, Sakthivel KM, Josephine C, et al (2025) Mechanistic insights into molecular targeted therapy and immunotherapy for lung cancer. *Biochemical and biophysical research communications* 776:152204. <https://doi.org/10.1016/j.bbrc.2025.152204>

Wu Y, Wang Y, Huang X, et al (2025) Multimodal learning for non-small cell lung cancer prognosis. *Biomedical Signal Processing and Control* 106:107663

Xu H, Usuyama N, Bagga J, et al (2024) A whole-slide foundation model for digital pathology from real-world data. *Nature* 630:181 – 188. <https://doi.org/10.1038/s41586-024-07441-w>

Yang H, Yang M, Chen J, et al (2024) Multimodal deep learning approaches for precision oncology: a comprehensive review. *Briefings in Bioinformatics* 26. <https://doi.org/10.1093/bib/bbae699>

Yang H, Wang J, Wang W, et al (2025) Mmsurv: a multimodal multi-instance multi-cancer survival prediction model integrating pathological images, clinical information, and sequencing data. *Briefings in Bioinformatics* 26. <https://doi.org/10.1093/bib/bbaef209>

Yuan X, Xu H, Zhu J, et al (2025) Systematic review and meta-analysis of artificial intelligence for image-based lung cancer classification and prognostic evaluation. *NPJ precision oncology* 9(1):300

Zhang S, Metaxas DN (2023) On the challenges and perspectives of foundation models for medical image analysis. *Medical image analysis* 91:102996. <https://doi.org/10.1016/j.media.2023.102996>

